



university of  
 groningen

faculty of mathematics  
 and natural sciences

kapteyn astronomical  
 institute



# Star Cluster Disruption in Dark Matter Dominated Galaxies

Anneke Praagman

Presented in fulfillment of the requirements  
 of the degree of Master of Science in Astronomy

August 30, 2008

Kapteyn Astronomical Institute  
 and  
 Swinburne University

Supervisors  
 Dr. Chris Power  
 Dr. Jarrod Hurley



# Acknowledgements

There are a few people that I would like to thank for a wonderful year I have spent at Swinburne to work on my master thesis. I would like to start by thanking the people that were involved in getting me there in the first place. First of all there is Nigel Douglas who offered the opportunity to go to Australia. At the other end there was Alistair Graham helping me to get things sorted in Australia.

Then of course both my supervisors Chris Power and Jarrod Hurley. Chris, thanks for taking me on as a student and helping me in every way you could. Even at the other side of the world you remained a source of inspiration from which many ideas emerged. You have taught me to be excited about results and I am looking forward to working with you again in the future. Jarrod, you were a great supervisor and mentor and I have learned a lot from you. Not just about the joys of  $N$ -body programming but also how to be a good and confident scientist. I know you were a bit "dissapointed to see an error of judgement in one of your students" but I hope that the Hawks will show you this weekend that I was right.

I would like to thank everyone at the Centre of Astrophysics and Supercomputing for making me feel welcome. In particular Caroline, you have been my 'best mate' from the first day we got to know each other. Adam, you were always there for me even at the busiest of times. Without you this year would not have been the same.

# Contents

<b>1</b>	<b>Introduction</b>	<b>6</b>
1.1	Globular clusters . . . . .	6
1.2	Globular clusters and galaxy formation . . . . .	6
1.3	Dark matter halos . . . . .	9
1.3.1	The Navarro, Frenk & White density profile . . . . .	9
1.4	Key aims of this thesis . . . . .	10
<b>2</b>	<b>The basics of <math>N</math>-body programming and a sample simulation</b>	<b>11</b>
2.1	Sample $N$ -body program . . . . .	11
2.1.1	Divided differences . . . . .	11
2.1.2	Integration . . . . .	13
2.1.3	Initial conditions . . . . .	15
2.2	$N$ -body units . . . . .	15
2.2.1	Conversion to physical units . . . . .	16
2.3	The Plummer model . . . . .	17
2.4	Test simulation with 1000 equal mass particles . . . . .	18
2.4.1	Spatial distribution . . . . .	19
2.4.2	Radial velocities . . . . .	19
2.4.3	Density distribution . . . . .	21
<b>3</b>	<b>The physics of stellar systems</b>	<b>23</b>
3.1	Physical parameters . . . . .	23
3.1.1	Relaxation time . . . . .	23
3.1.2	Half-mass relaxation time . . . . .	26
3.1.3	Core radius . . . . .	26
3.1.4	Tidal radius . . . . .	27
3.1.5	Collisionless systems and the virial theorem . . . . .	28
3.1.6	Heat capacity in self-gravitating systems and the gravothermal catastrophe . . . . .	28
3.2	Evolution trends in spherical systems . . . . .	29
3.2.1	Evaporation and Ejection . . . . .	29

3.2.2	Core collapse . . . . .	30
3.2.3	Equipartition . . . . .	30
3.2.4	Binary formation . . . . .	30
<b>4</b>	<b>nbody6</b>	<b>32</b>
4.1	Hermite integration . . . . .	32
4.2	Time-steps . . . . .	33
4.2.1	Improved time-step criterion . . . . .	33
4.2.2	Block time-steps . . . . .	33
4.3	Other important additions . . . . .	33
4.3.1	Binary formation and hierarchical systems . . . . .	33
4.3.2	Neighbour scheme . . . . .	34
4.3.3	Stellar evolution . . . . .	34
4.3.4	External tidal fields . . . . .	34
4.4	Hardware . . . . .	35
4.5	Input file and user options . . . . .	35
4.6	Other methods . . . . .	36
<b>5</b>	<b>Results using existing options</b>	<b>37</b>
5.1	Simulations with nbody6 . . . . .	37
5.1.1	Results using nbody6 . . . . .	38
<b>6</b>	<b>Including a nfw dark matter halo</b>	<b>48</b>
6.1	The Navarro, Frenk and White density profile . . . . .	48
6.2	Addition of NFW halo to nbody6 . . . . .	49
6.3	Cartesian coordinates . . . . .	50
6.4	Addition to the code . . . . .	51
6.5	Experiments . . . . .	51
6.5.1	Adding the disk + bulge . . . . .	51
6.5.2	The evolution of the cluster in a pure NFW halo . . . . .	52
6.5.3	Putting the galaxy in the halo . . . . .	58
<b>7</b>	<b>The generalized NFW profile</b>	<b>61</b>
7.1	Generalized NFW profile . . . . .	61
7.2	Addition to nbody6 . . . . .	65
7.3	Results . . . . .	65
<b>8</b>	<b>Conclusions</b>	<b>69</b>
8.1	Future work . . . . .	70
<b>A</b>	<b>Comparison of identical models with different random number seeds</b>	<b>71</b>

# Chapter 1

## Introduction

### 1.1 Globular clusters

Globular clusters are compact stellar systems each containing of order  $10^6$  stars that are found in the outskirts of galaxies, most of them on highly eccentric orbits. Our Galaxy has about 200 globular clusters and observations show that almost all galaxies host these systems with giant ellipticals appearing to have the largest (relative) populations of globular clusters. Stellar population studies show that the age of globular clusters is around 13 Gyrs (e.g. Hansen et al. 2002; Chaboyer & Krauss 2002) comparable to the age of the Universe (e.g. Spergel et al. 2007). Evidently these clusters are very old and were likely born in the early phases of galaxy formation. Globular clusters span a range in metallicities. From extragalactic studies it has become clear that there is a bimodality in their colour distribution suggesting two classes of globular clusters - metal poor and metal rich. Most globular clusters are nearly spherical and some of them show a central cusp. For a detailed discussion of globular cluster see Spitzer (1987) and Brodie & Strader (2006).

### 1.2 Globular clusters and galaxy formation

The metal poor population of globular clusters are extremely interesting from a cosmological perspective. They are believed to have formed within  $\sim 1$  billion years of the Big Bang and therefore represent a fossil record of the earliest epoch of galaxy formation. As such, they are potentially powerful probes of physical conditions in the high redshift Universe. However, there is as yet no compelling theory for the formation of globular clusters within a cosmological framework, and this has important consequences for (a) how

we interpret the fossil record and (b) the strength of conclusions that we can draw from it.

The standard paradigm of galaxy formation asserts that galaxies form when gas cools and forms stars within the deep potential wells of massive structures of dark matter that are referred to as *dark matter halos* (cf. White & Rees 1978). These dark matter halos assemble in a hierarchical manner, continuously growing via accretion and merging from high redshift to the present day. The formation and evolution of dark matter halos has been studied in exhaustive detail using cosmological simulations, and the process is relatively well understood. This has led to a well developed theory, the Cold Dark Matter model, and it is within this framework that galaxy formation is investigated (cf. Springel et al. 2006). However, galaxy formation - and consequently globular cluster formation - is much more complex, and there remain many outstanding problems.

There are a number of well developed galaxy formation models now available, and their key features are summarised in, for example, Baugh (2006). These models tend to focus on reproducing statistical properties of the galaxy population at low-to-intermediate redshifts, such as their colours and luminosities (eg. Bower et al. 2006; Croton et al. 2006). In contrast, relatively little has been done on modeling globular cluster formation. Kravtsov & Gnedin (2005) used cosmological simulations of the formation of a disc galaxy to argue that globular clusters form in massive molecular clouds embedded in the gas-rich proto-galactic disc. Taniguchi et al. (1999) speculated that shells of material swept up by outflows driven by the growing central black hole in the proto-galaxy could fragment into globular clusters. Others have speculated that mergers between gas-rich discs at high redshifts could result in globular clusters, analogues of the super-star clusters observed in mergers in the local Universe.

The nature of the formation site could have a profound effect on the structural and orbital properties of the globular cluster that forms. For example, the chemical composition of material in the disc will likely differ from that of material in a swept-up shell; this will affect the rate at which gas absorbs and radiates energy and therefore could impact on the initial mass function of cluster stars and consequently mass segregation within the cluster. However, independent of precisely how and where globular clusters form, they subsequently evolve orbiting a galaxy embedded in a dark matter halo. The central question of this work is to *ask how the structure of the dark matter halo affects the time evolution of the globular cluster*.

Over its lifetime, a globular cluster loses mass. This mass loss will depend on processes within the cluster (e.g. core collapse, binary formation, stellar

evolution), but it will also be sensitive to the external potential within which it orbits. This problem has been studied in detail for a particular set of galactic potentials (e.g. Giersz & Heggie 1997; Hurley et al. 2007). However not only are these galactic models very simplistic describing the galaxy as a point source, they do not address dark matter halos at all. Mashchenko & Sills (2005) do address dark halos but they look at the effect of the dark matter *in* the globular cluster itself. In this study I wish to investigate the problem using potentials motivated by a cosmological framework. This is significant in that it may contribute to answer the following outstanding questions.

Can we use the present day metal poor population to deduce the efficiency of globular cluster formation - and more generally star formation - at high redshifts? A census of metal poor globular clusters around a particular galaxy could in principle reveal this information, provided we understood how many globular clusters were disrupted over the lifetime of the galaxy. If the rate of disruption is strongly dependent on the nature of the dark matter potential, then it is conceivable that the population we observe today might just be the “tip of the iceberg” (the initial iceberg at least). Interestingly, if globular clusters are too efficiently disrupted in particular kinds of potential to be consistent with observation, given even the most optimistic formation efficiencies, one could rule out these potentials.

Debris from disrupted globular clusters could be an important contribution to the stellar halos of galaxies. Such halos would have steep density profiles, because the disruption of the progenitor clusters happened early in the galaxy’s assembly history, and we might expect them to be relatively metal poor, reflecting the nature of their origin. This may help explain recent results from projects such as GHOSTS, an HST legacy survey, which is exploring the structural properties of 14 nearby disc galaxies. Initial results indicate that the typical stellar halo is too steep to be explained by satellite accretions. Could the disruption of a subset of the initial globular cluster population produce a stellar halo consistent with observation?

It is generally assumed that globular clusters do not contain dark matter. Dark matter would provide dynamical stability over the cluster’s lifetime, especially in the presence of an external potential, and could prevent their disruption. If the rate of disruption is too great in cosmologically motivated dark matter potentials, might this be remedied if globular clusters formed and evolved initially in their own dark matter halos?

## 1.3 Dark matter halos

Dark matter halos that form in cosmological simulations are relatively complex structures - they are generally aspherical (e.g. Bailin & Steinmetz 2005) and asymmetric (e.g. Gao & White 2006) with no simple boundary (e.g. Prada et al. 2006), and they contain a wealth of small scale structure (Gao et al. 2004). Despite this complexity, it is conventional to identify a halo as a spherical volume enclosing a mean overdensity that is *some multiple* of the background density of the Universe. The mass enclosed within this spherical volume defines the *virial mass* of the halo,

$$M_{\text{vir}} = \frac{4\pi}{3} \Delta_{\text{vir}} \rho_{\text{crit}} r_{\text{vir}}^3. \quad (1.1)$$

Here  $\rho_{\text{crit}} = 3H^2/8\pi G$  is the critical density of the Universe and  $r_{\text{vir}}$  is the *virial radius*, which defines the radial extent of the halo.  $\Delta_{\text{vir}}$ , the virial overdensity criterion, is *some multiple* of the background density, and corresponds to the mean overdensity at the time of virialisation in the spherical collapse model, the simplest analytic model of halo formation (cf. Eke et al. 1996). Depending on redshift and cosmological parameters,  $\Delta_{\text{vir}}$  varies between  $\sim 100$  and  $\sim 200$ .

The mass profiles of dark matter halos forming in cosmological  $N$ -body simulations have been studied in exhaustive detail since the mid 1990s (e.g. Navarro, Frenk & White 1995, 1996; Moore et al. 1998; Navarro et al. 2004; Diemand et al. 2005). The mass profile measures the variation of the spherically averaged local density with respect to distance from the centre of the dark matter halo. A common feature of all dark matter models is that the local dark matter density increases with decreasing radius and continues to diverge at small radii, down to the resolution limit of the simulations. The Navarro, Frenk & White (1996, 1997) mass profile is a good approximation to the mass profile of cosmological dark matter halos. I describe it briefly in the following subsections.

### 1.3.1 The Navarro, Frenk & White density profile

The spherically averaged mass profile proposed by Navarro, Frenk & White (1996, 1997) can be written as

$$\rho(r) = \frac{\rho_{\text{crit}} \delta_c}{r/r_s (1 + r/r_s)^2}, \quad (1.2)$$

where  $\rho_{\text{crit}}$  is the critical density of the Universe,  $r_s$  is the scale radius and  $\delta_c$  is the characteristic overdensity. The Navarro, Frenk & White (hereafter

NFW) functional form provides a good approximation to the mass profiles of dark matter halos in dynamical equilibrium that form in cosmological simulations. The key characteristic of the NFW profile is that the density diverges at small radii as  $r^{-1}$ , resulting in a central density *cusp*.

The scale radius  $r_s$  and the characteristic overdensity  $\delta_c$  are related, and equation 1.2 can be rewritten in terms of a single parameter, the concentration  $c = r_{\text{vir}}/r_s$ , such that for a fixed concentration, the local density depends only on the normalised radius  $r/r_{\text{vir}}$ . Cosmological simulations have shown that virial mass  $M_{\text{vir}}$  and concentration  $c$  are correlated, such that the concentration increases as the virial mass decreases (e.g. Bullock et al. 2001, Eke et al. 2001, Neto et al. 2007). Further information on the NFW profile can be found in Chapter 6.

The characteristic feature of the NFW profile is its central logarithmic asymptotic slope of -1. However, it is interesting to rewrite equation 1.2 in the form

$$\rho(r) = \frac{\rho_{\text{crit}}\delta_c}{(r/r_s)^\alpha (1 + r/r_s)^{3-\alpha}}, \quad (1.3)$$

such that the central logarithmic asymptotic slope  $\alpha$  can vary in principle between 0 and  $-3$ , while the outer logarithmic slope continues to asymptote to  $-3$  at large radii. More details will be given in Chapter 7

## 1.4 Key aims of this thesis

It is expected that under the influence of the external tidal field globular clusters lose mass and may even disrupt. I want to study this disruption by applying various tidal fields to the cluster with an emphasis on the effects of a dark matter halo. I use the NFW profile to probe the impact of halo mass and degree of concentration and use its generalised form to investigate the effect of the inner slope.

In Chapter 2 I introduce the fundamental elements of the  $N$ -body program used to model star cluster evolution and show a few results for a very simple model. In Chapter 3 I discuss the physical processes that a star cluster is subject to over its lifetime. Chapter 4 is a short introduction to a more extensive  $N$ -body code, `nbody6`, which I will use to follow the long-term evolution of star clusters. I then go on to discuss results for the evolution of a star cluster using existing options in `nbody6` in Chapter 5. Results for simulations run with an added option for a NFW profile and generalised NFW profile are discussed in Chapters 6 and 7 respectively.

# Chapter 2

## The basics of $N$ -body programming and a sample simulation

### 2.1 Sample $N$ -body program

To build some intuition about  $N$ -body programming and for the physical processes involved in the evolution of globular clusters I ran a test simulation using Aarseth's Standard  $N$ -Body Program `nbody1` obtained from Binney & Tremaine (1987). It was written by S.J. Aarseth, whose programs have set the industry standard in this area for many years. The program computes the time evolution of  $N$  point masses under the influence of their mutual self-gravity. The acceleration of each mass is computed by the direct summation of the forces arising from the other  $N - 1$  bodies, so the computation time per crossing time grows roughly as  $N^2$ . A key strategy of the program is that each particle is followed with its own time-step - an essential feature in view of the wide range of orbital times in a typical stellar system.

The direct integration scheme used is the traditional polynomial method with individual time-steps which makes use of Newton's divided differences as explained in this section following Aarseth (1994).

#### 2.1.1 Divided differences

The equation of motion for each particle  $i$  is:

$$\ddot{\mathbf{r}}_i = -G \sum_{\substack{j=1 \\ j \neq i}}^N \frac{m_j (\mathbf{r}_i - \mathbf{r}_j)}{((|\mathbf{r}_i - \mathbf{r}_j|)^2 + \epsilon^2)^{3/2}}, \quad (2.1)$$

where  $m_j$  is the mass of each particle ( $j = 1, N$ ). The softening parameter  $\epsilon$  prevents a force singularity as the distance  $r_{ij}$  between two particles  $i$  and  $j$  with positions  $\mathbf{r}_i$  and  $\mathbf{r}_j$  goes to zero. Using scaled units (see Section 2.2) the gravitational constant  $G$  is set to one. Defining the left hand side of equation 2.1 as the force per unit mass  $\mathbf{F}$  on particle  $i$  (omitting the subscript), the fourth-order fitting polynomial from Newton's divided difference method at time  $t$  is written as<sup>1</sup>

$$\mathbf{F}_t = (((\mathbf{D}^4(t - t_3) + \mathbf{D}^3)(t - t_2) + \mathbf{D}^2)(t - t_1) + \mathbf{D}^1)(t - t_0) + \mathbf{D}^0, \quad (2.2)$$

provided the forces are known at the four successive past epochs  $t_3, t_2, t_1$ , and  $t_0$ , with  $t_0$  being the most recent. The divided differences  $\mathbf{D}^k$  are defined by:

$$\mathbf{D}^k[t_0, t_k] = \frac{\mathbf{D}^{k-1}[t_0, t_{k-1}] - \mathbf{D}^{k-1}[t_1, t_k]}{t_0 - t_k}; \quad (k = 1, 2, 3), \quad (2.3)$$

where  $\mathbf{D}^0 \equiv \mathbf{F}$ . At the start of an integration step the fourth difference,  $\mathbf{D}^4$ , is not yet known. This has to be deduced from the force at time  $t$  which will be computed during the integration so that the term  $\mathbf{D}^4$  is added at the end of an integration step in a process called 'semi-iteration'. The calculation of  $\mathbf{D}^4$  will be explained at the end of this section.

Initially there are no known past epochs. In order to find values for the initial differences the force polynomial (equation 2.2) is expanded in a Taylor series around  $t = t_0$  to yield the force derivatives:

$$\begin{aligned} \mathbf{F}^{(1)} &= ((\mathbf{D}^4(t_0 - t_3) + \mathbf{D}^3)(t_0 - t_2) + \mathbf{D}^2)(t_0 - t_1) + \mathbf{D}^1 \\ \mathbf{F}^{(2)} &= 2! (\mathbf{D}^4((t_0 - t_1)(t_0 - t_2) + (t_0 - t_2)(t_0 - t_3) + (t_0 - t_1)(t_0 - t_3)) \\ &\quad + \mathbf{D}^3((t_0 - t_1) + (t_0 - t_2)) + \mathbf{D}^2) \\ \mathbf{F}^{(3)} &= 3! (\mathbf{D}^4((t_0 - t_1) + (t_0 - t_2) + (t_0 - t_3)) + \mathbf{D}^3) \\ \mathbf{F}^{(4)} &= 4! \mathbf{D}^4. \end{aligned} \quad (2.4)$$

These equations can be inverted to third order (since the fourth difference is still unknown) to create starting values for the divided differences:

$$\begin{aligned} \mathbf{D}^1 &= \left(\frac{1}{6}\mathbf{F}^{(3)}(t_0 - t_1) - \frac{1}{2}\mathbf{F}^{(2)}(t_0 - t_1) + \mathbf{F}^{(1)}\right) \\ \mathbf{D}^2 &= -\frac{1}{6}\mathbf{F}^{(3)}((t_0 - t_1)(t_0 - t_2)) + \frac{1}{2}\mathbf{F}^{(2)} \\ \mathbf{D}^3 &= \frac{1}{6}\mathbf{F}^{(3)}, \end{aligned} \quad (2.5)$$

---

<sup>1</sup>For a detailed description of the divided differences see e.g. chapter 3.2 of Burden & Faires (2001)

where  $t_1$  and  $t_2$  are set to be two past epochs equally spaced in time. Denoting  $\mathbf{R} = \mathbf{r}_i - \mathbf{r}_j$  (including softening) and  $\mathbf{V} = \mathbf{v}_i - \mathbf{v}_j$ , the velocity difference between two particles, for each pair  $i, j$  the force (per unit mass) and its derivatives from equation 2.1 are (still using scaled units)

$$\begin{aligned}
\mathbf{F}_{ij} &= -\frac{m_j \mathbf{R}}{R^3} \\
\mathbf{F}_{ij}^{(1)} &= -\frac{m_j \mathbf{V}}{R^3} - 3a \mathbf{F}_{ij} \\
\mathbf{F}_{ij}^{(2)} &= -\frac{m_j (\mathbf{F}_i - \mathbf{F}_j)}{R^3} - 6a \mathbf{F}_{ij}^{(1)} - 3b \mathbf{F}_{ij} \\
\mathbf{F}_{ij}^{(3)} &= -\frac{m_j (\mathbf{F}_i^{(1)} - \mathbf{F}_j^{(1)})}{R^3} - 9a \mathbf{F}_{ij}^{(2)} - 9b \mathbf{F}_{ij}^{(1)} - 3c \mathbf{F}_{ij},
\end{aligned} \tag{2.6}$$

with

$$\begin{aligned}
a &= \frac{\mathbf{R} \cdot \mathbf{V}}{R^2} \\
b &= \left(\frac{V}{R}\right)^2 + \frac{\mathbf{R} \cdot (\mathbf{F}_i - \mathbf{F}_j)}{R^2} + a^2 \\
c &= \frac{3\mathbf{V} \cdot (\mathbf{F}_i - \mathbf{F}_j)}{R^2} + \frac{\mathbf{R} \cdot (\mathbf{F}_i^{(1)} - \mathbf{F}_j^{(1)})}{R^2} + a(3b - 4a^2).
\end{aligned}$$

Here  $\mathbf{F}_i$  is the total force on particle  $i$ . The second and third derivatives use the total force and total force derivative respectively and they thus have to be calculated in an additional loop. These values can then be used to find the initial differences from equation 2.5.

## 2.1.2 Integration

After the initial difference values have been set the integration starts. The basic integration cycle consists of the following steps:

1. Find the next body  $i$  to be advanced and set new global time  $t$ ;
2. Predict positions of all bodies to order  $\mathbf{F}^{(1)}$ ;
3. Form  $\mathbf{F}^{(2)}$  and  $\mathbf{F}^{(3)}$  from divided differences for body  $i$ ;
4. Determine position and velocity for body  $i$  to order  $\mathbf{F}^{(3)}$ ;
5. Find new total force on body  $i$ ;

6. Update times  $t_k$  and differences  $\mathbf{D}^k$ ;
7. Apply fourth order correction  $\mathbf{D}^4$ ; and,
8. Set new time step  $\Delta t_i$ .

### Time step

A typical stellar system is characterized by a range in density which gives rise to different time scales for significant changes of the orbital parameters. It is thus efficient to assign each particle  $i$  its own time step related to its orbital time scale which is determined by

$$\Delta t_i = \left( \eta \frac{F}{F^{(2)}} \right)^{1/2}, \quad (2.7)$$

where  $\eta$  is an accuracy parameter, typically set to about 0.02. The particle that needs to be updated next is the one that has the smallest  $t = t_i + \Delta t_i$  where  $t_i$  is the time it was last updated and the time  $t$  is now called the global time.

### Coordinate prediction

Each particle is affected by all other particles and thus a temporary coordinate prediction for all particles is needed at the global time  $t$  to determine the current force on the particle to be advanced. High precision is not ordinarily required so this prediction is done to order  $\mathbf{F}^{(1)}$  to save computing time:

$$\mathbf{r}_t = \left( \left( \frac{1}{3!} \mathbf{F}^{(1)}(t - t_0) + \frac{1}{2!} \mathbf{F} \right) (t - t_0) + \mathbf{v}_0 \right) (t - t_0) + \mathbf{r}_0, \quad (2.8)$$

where  $t_0$  for each particle is the time it was last updated.

For the particle to be advanced the position and velocity are determined more accurately to third order in force:

$$\mathbf{r}_t = \left( \left( \left( \left( \frac{1}{5!} \mathbf{F}^{(3)}(t - t_0) + \frac{1}{4!} \mathbf{F}^{(2)} \right) (t - t_0) + \frac{1}{3!} \mathbf{F}^{(1)} \right) (t - t_0) + \frac{1}{2!} \mathbf{F} \right) (t - t_0) + \mathbf{v}_0 \right) (t - t_0) + \mathbf{r}_0 \quad (2.9)$$

$$\mathbf{v}_t = \left( \left( \left( \frac{1}{4!} \mathbf{F}^{(3)} \right) (t - t_0) + \frac{1}{3!} \mathbf{F}^{(2)} \right) (t - t_0) + \frac{1}{2!} \mathbf{F}^{(1)} \right) (t - t_0) + \mathbf{F} (t - t_0) + \mathbf{v}_0, \quad (2.10)$$

where the forces and force derivatives have been determined from equation 2.4 to third order since the forces at time  $t$  are still unknown.

### Find force and update times and differences

From the predicted positions the total current force on the body of interest can be determined (equation 2.1). Then the times for body  $i$  can be updated:

$$t_2 \rightarrow t_3, \quad t_1 \rightarrow t_2, \quad t_0 \rightarrow t_1, \quad t \rightarrow t_0,$$

and the new differences determined from equation 2.3. At this time the force is known at the present epoch and four successive past epochs. Thus the fourth difference can now be determined and used to obtain more accuracy on the position and velocity of body  $i$ :

$$\mathbf{D}^4[t, t_3] = \frac{\mathbf{D}^3[t, t_2] - \mathbf{D}^3[t_0, t_3]}{t - t_3}, \quad (2.11)$$

with

$$\mathbf{D}^k[t, t_{k-1}] = \frac{\mathbf{D}^{k-1}[t, t_{k-2}] - \mathbf{D}^{k-1}[t_0, t_{k-1}]}{t - t_{k-1}}. \quad (2.12)$$

Finally the new time step for body  $i$  is determined by equation 2.7.

### 2.1.3 Initial conditions

To start the  $N$ -body simulation a starting model is needed which provides the mass, initial position and velocity for each star. The code to generate this model was adapted from algorithms in `nbody6` (see Chapter 4). The input parameters are the number of bodies  $N$ , the initial mass function (IMF), density model (such as the Plummer model, see Section 2.3) and half-mass radius. It generates a file containing mass, position and velocity for each body in either  $N$ -body or physical units.

## 2.2 $N$ -body units

To scale the output of a simulation there are three free parameters (mass, length, time) to define the units. There is no official standard but a widely used scheme for computer simulations in stellar dynamics is setting

$$G = M = r_V = 1,$$

where  $G$ ,  $M$  and  $r_V$ , are the gravitational constant, total mass of the system and the virial radius respectively (Aarseth 2003). The virial radius is defined such that

$$\frac{M^2}{r_V} = \sum_i \sum_{\substack{j \\ j \neq i}} \frac{m_i m_j}{|\mathbf{r}_i - \mathbf{r}_j|}. \quad (2.13)$$

These are generally referred to as 'standard units' (Heggie & Mathieu 1986) or sometimes 'Heggie units'.

The fourth 'Heggie unit' is the total energy which can be derived from the other three. Apart from a minus sign equation 2.13 is twice the potential energy of the  $N$ -body system with  $G = 1$  since all pairs are doubly counted. So the potential energy of the  $N$ -body system can be written as:

$$W = -G \sum_{i < j} \frac{m_i m_j}{|\mathbf{r}_i - \mathbf{r}_j|} = -\frac{1}{2} \frac{GM^2}{r_V}. \quad (2.14)$$

The scalar virial theorem ( $2K + W = 0$ ) gives

$$E_{tot} = \frac{1}{2}W = -\frac{1}{4} \frac{GM^2}{r_V}. \quad (2.15)$$

Using the first three Heggie units this results in an  $N$ -body total energy of -0.25.

## 2.2.1 Conversion to physical units

To compare the results of an  $N$ -body simulation with other models or observations, the computed quantities should be scaled to meaningful astrophysical quantities. The scaling of mass and distance is straightforward. In  $N$ -body units the total mass  $M$  and the virial radius  $r_V$  are equal to 1. If the total physical mass of the system is  $\tilde{M}$  and the physical virial radius is  $\tilde{r}_V$  then mass ( $\tilde{m}$ ) and distance ( $\tilde{r}$ ) in physical units are obtained from the  $N$ -body units by

$$\tilde{m} = \tilde{M}m \quad (2.16)$$

and

$$\tilde{r} = \tilde{r}_V r. \quad (2.17)$$

For globular clusters a natural mass scale is the solar mass ( $M_\odot$ ) and a natural length scale is the parsec (pc). Their SI-values are listed in Table 2.1. The user chooses a physical total mass and virial radius for the cluster and together with the known value for  $G$  this determines the conversion factors for all other parameters. The conversion of the time and the velocity units is a bit more complicated. A dimensional analysis yields for the time ( $[\tilde{t}]$ ) and velocity ( $[\tilde{v}]$ ) physical units

$$[\tilde{t}] = \left( \frac{[\tilde{r}]^3}{G[\tilde{m}]} \right)^{1/2} \quad (2.18)$$

Astrophysical unit	Value in SI-units
$M_{\odot}$	$1.99892 \times 10^{30}$ kg
pc	$3.08568 \times 10^{16}$ m
$G$	$6.67 \times 10^{-11}$ m <sup>3</sup> kg <sup>-1</sup> s <sup>-2</sup>

Table 2.1: Values of useful astrophysical quantities.

$$[\tilde{v}] = \left( \frac{G[\tilde{m}]}{[\tilde{r}]} \right)^{1/2}. \quad (2.19)$$

Using the relations from equations 2.16 and 2.17 with units  $M_{\odot}$  and  $r_V$  this results in

$$[\tilde{t}] = \left( \frac{\tilde{r}_V^3}{\tilde{M}} \right)^{1/2} \left( \frac{\text{pc}^3}{GM_{\odot}} \right)^{1/2} = 14.94 \left( \frac{\tilde{r}_V^3}{\tilde{M}} \right)^{1/2} \text{ Myr} \quad (2.20)$$

$$[\tilde{v}] = \left( \frac{\tilde{M}}{\tilde{r}_V} \right)^{1/2} \left( \frac{GM_{\odot}}{\text{pc}} \right)^{1/2} = 0.06557 \left( \frac{\tilde{M}}{\tilde{r}_V} \right)^{1/2} \text{ km/s}. \quad (2.21)$$

## 2.3 The Plummer model

To fit observations of globular clusters Plummer (1911) used the following potential-density pair:

$$\Phi(r) = -\frac{GM}{\sqrt{r^2 + b^2}} \quad (2.22)$$

$$\rho(r) = \left( \frac{3M}{4\pi b^3} \right) \left( 1 + \frac{r^2}{b^2} \right)^{-\frac{5}{2}}, \quad (2.23)$$

where  $b$  is the scale length of the system. The total potential energy of a system is the sum of the energies that each particle feels with respect to the other particles divided by two because of double counting. So this becomes

$$W = \frac{1}{2} \int_0^{\infty} \Phi(r) \rho(r) 4\pi r^2 dr = -\frac{3\pi}{32} \frac{GM^2}{b}. \quad (2.24)$$

This can then be related to the potential energy from equation 2.14 to find an expression for the scale length in  $N$ -body units

$$b = 0.59.$$

Another quantity often used to describe the scale of a system is the half-mass radius. It is defined as the radius containing half the mass:

$$\int_0^{r_h} \rho(r)r^2 dr = \int_{r_h}^{\infty} \rho(r)r^2 dr. \quad (2.25)$$

This can be computed using Poisson's equation for spherical symmetry:

$$\frac{d^2\Phi}{dr^2} + \frac{2}{r} \frac{d\Phi}{dr} = 4\pi G\rho(r), \quad (2.26)$$

after some algebra resulting in

$$2r_h^2 \frac{d\Phi(r_h)}{dr} = \lim_{r \rightarrow \infty} r^2 \frac{d\Phi(r)}{dr}. \quad (2.27)$$

Using the Plummer potential from equation 2.22 this gives

$$r_h \approx 1.30b.$$

In  $N$ -body units

$$r_h = 0.77$$

for the Plummer model (Aarseth & Fall 1980).

This model is commonly used as the density model for generating  $N$ -body initial conditions, primarily because of its mathematical simplicity. Other models exist, such as the King model (King 1966) which have been shown to better represent the profiles of observed globular clusters. However, an initial distribution based on the Plummer model will over time dynamically evolve to represent a King model (Hurley & Shara 2003).

## 2.4 Test simulation with 1000 equal mass particles

Here I show the results of a sample simulation using 1000 solar mass stars which are initial distributed based on the Plummer model and have a virial radius of 3 parsec. This means that a  $N$ -body time unit is equivalent to 2.45 Myr (c.f. equation 2.18). The typical age of a globular cluster is of the order of 10 Gyr. Thus the integration is done over roughly 4000  $N$ -body time units.

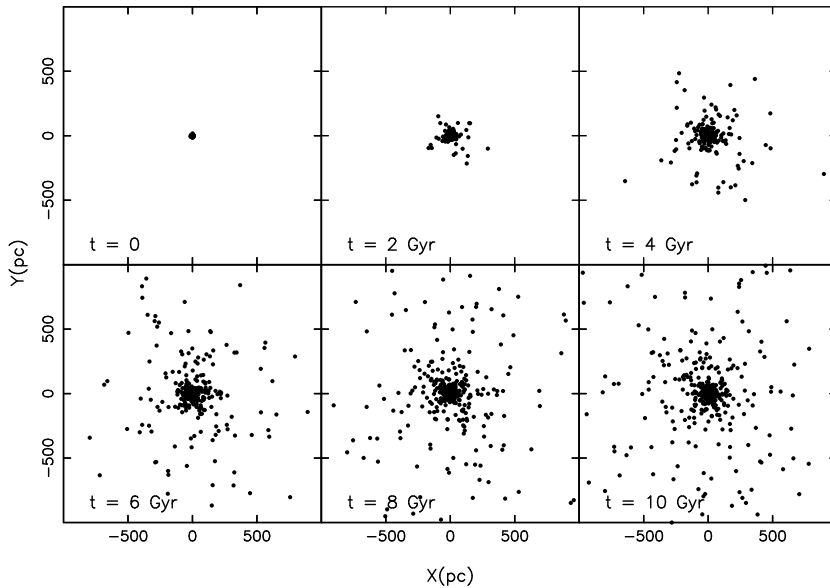


Figure 2.1: The evolution of the projected spatial distribution of the stars in the cluster. As the cluster evolves a few stars move outside the boxes shown in these figures extending as far out as 7000 pc at 10 Gyr but they are not drawn here for reasons of resolution.

### 2.4.1 Spatial distribution

Figure 2.1 shows the evolution of the spatial stellar distribution projected onto the  $xy$ -plane over a period of 10 Gyr. It is clear that the system as a whole expands. Zooming in on the centre in Figure 2.2, however, shows that the core collapses inwards. Thus a distinct core-halo structure is established where a diffuse halo surrounds a high-density core.

This behaviour of core collapse and expansion of the outer envelope is also evident from Figure 2.3 where the radius containing a certain fraction of the mass is plotted versus time. We see clearly that over time the outer regions move outwards while the inner regions move inwards. This process will be further discussed in Section 3.2.

### 2.4.2 Radial velocities

The evolution of the radial velocities versus radius is shown in Figure 2.4. Stars in the outer regions have positive radial velocities, thus moving further away from the cluster. The velocity dispersion is small. In the core the average velocity is small but the dispersion is large. This is due to the fact

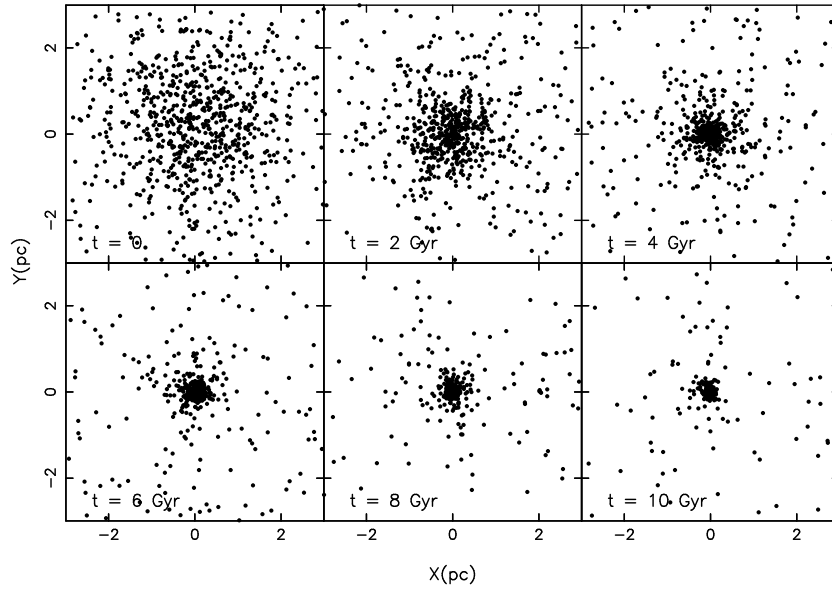


Figure 2.2: The evolution of the projected spatial distribution of the stars in the central 3 pc of the cluster.

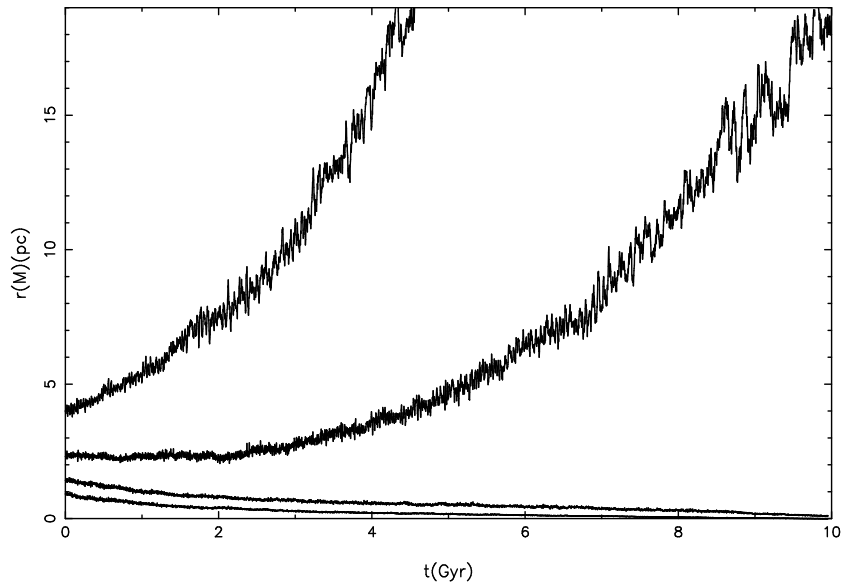


Figure 2.3: Radius containing (from top to bottom) 75%, 50%, 25% and 10% of the mass fraction evolving over time.

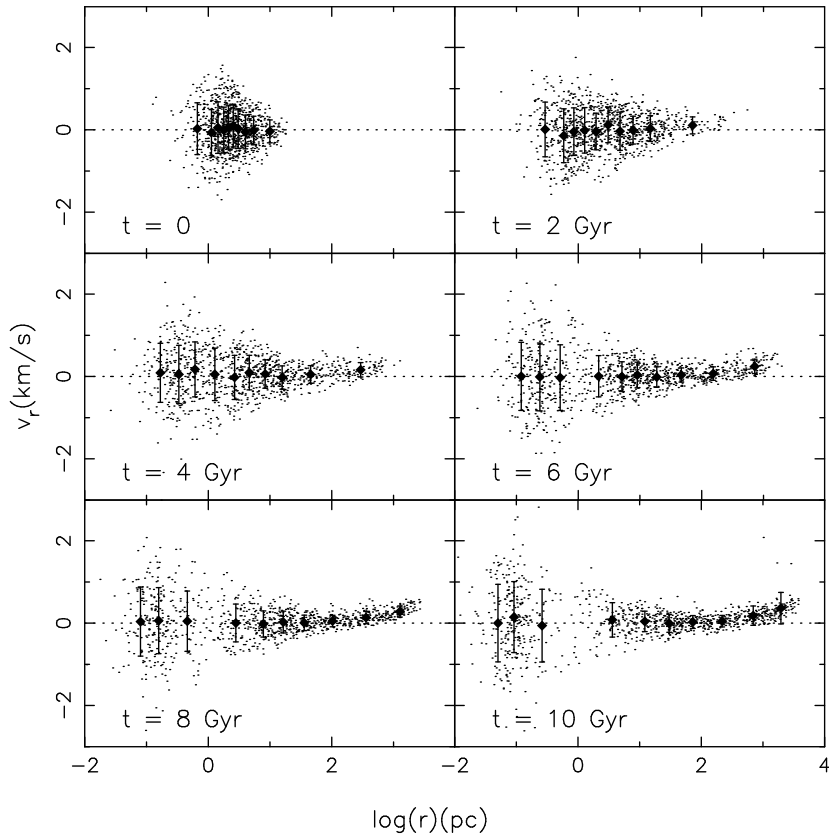


Figure 2.4: The evolution of the radial velocity distribution. The small dots represent the individual stars and the solid diamonds represent the binned data with  $1\sigma$  errorbars shown.

that stars in the core still interact heavily with each other while stars in the outer regions start seeing the rest of the cluster more and more as a point source as they move further out. In this figure the core-halo structure can be seen to develop as well.

### 2.4.3 Density distribution

In Figure 2.5 the evolution of the radial density distribution is shown. From an initial Plummer model stars in the centre start moving inward (core collapse), heightening the density and the envelope expands much further out, lowering the density in the outer regions. As the cluster evolves a Plummer model no longer represents the data well. More elaborate models such as the earlier mentioned King model are needed.

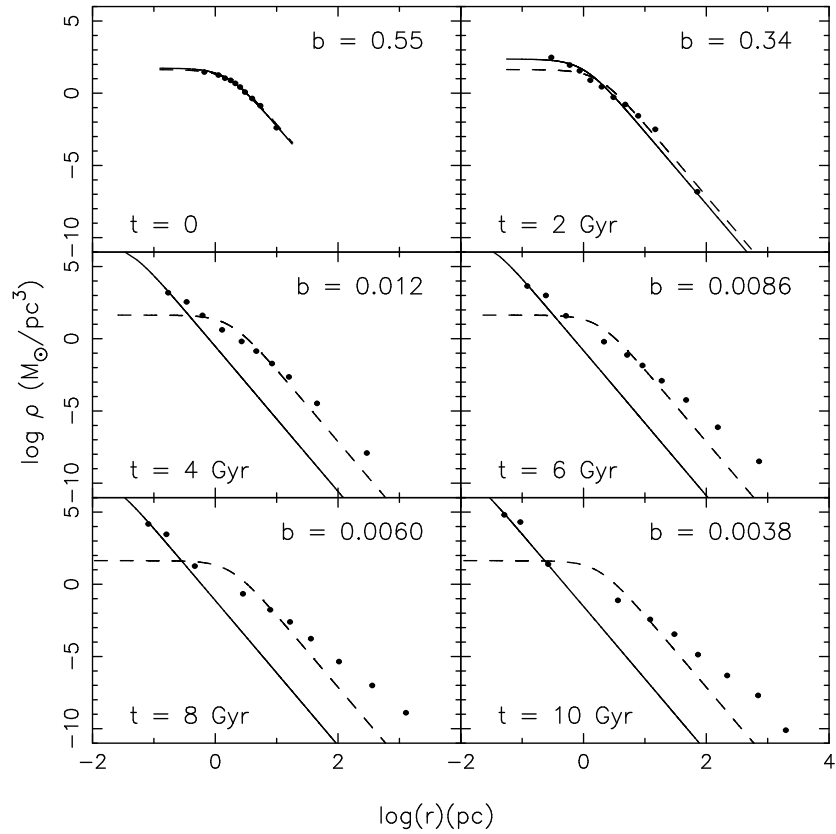


Figure 2.5: Radial density distribution evolution. The dots are the densities determined from the binned data. The solid line is the least square fitted Plummer model to the data with values of  $b$  listed in the top right hand corner. Also shown is the initial theoretical Plummer model with  $b = 0.59$  as a dashed line.

# Chapter 3

## The physics of stellar systems

In Chapter 2 I showed the results of a sample simulation using Aarseth's standard  $N$ -body program. In that model I saw the effects of a collapsing core and an expanding halo but I did not comment on the physical background for these processes. In this chapter I introduce some basic concepts that help define the underlying physics. I then discuss the main physical processes that play a role in the evolution of spherical systems. Looking ahead, this framework will facilitate the explanation of results of more elaborate models obtained using the `nbody6` (see Chapters 4 and 5) program

### 3.1 Physical parameters

In this section I introduce physical concepts needed to understand the evolution of a star cluster. Unless stated otherwise the background material for this chapter is taken from Binney & Tremaine (1987).

#### 3.1.1 Relaxation time

The relaxation time in a stellar system is a measure of the time it takes for an object in that system to be significantly perturbed by the other stars. It is then said to have "lost its memory" about its original state. On this timescale only weak encounters play a role. Stars are only influenced by the mean potential resulting from all the other stars. The relaxation time  $t_r$  is defined as the number of crossings needed to change the velocity squared by of order itself multiplied by the crossing time  $t_c = R/v$ , where  $R$  is the typical size of the system and  $v$  the typical speed of a star in that system. Consider a system of  $N$  stars of equal mass  $m$ . The change in velocity a test star experiences when it is gravitationally perturbed by another star (a field

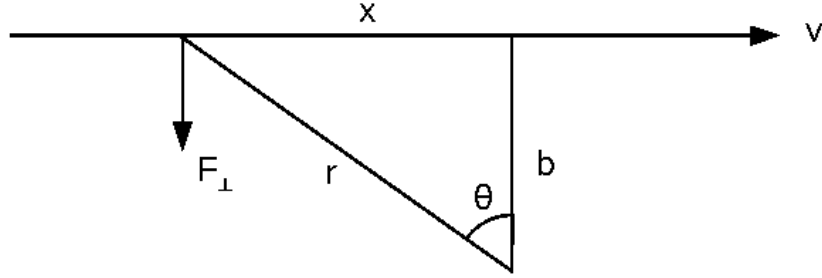


Figure 3.1: The test star approaches a field star at speed  $v$  and impact parameter  $b$ . The resulting impulse to the test star is estimated by approximating its trajectory as a straight line (Binney & Tremaine 1987).

star) can be envisaged as in Figure 3.1. The shortest distance between the two stars is the impact parameter  $b$ . Assume that the change in velocity  $v$  is small (i.e.  $|\delta\mathbf{v}|/v \ll 1$ ) so the trajectory of the star can be approximated by a straight line. The perpendicular velocity component  $\delta\mathbf{v}_\perp$  can be obtained by integrating the perpendicular force per mass  $m$

$$F_\perp = \frac{Gm}{b^2 + x^2} \cos\theta = \frac{Gmb}{(b^2 + x^2)^{3/2}} \simeq \frac{Gm}{b^2} \left[ 1 + \left( \frac{vt}{b} \right)^2 \right]^{-3/2}. \quad (3.1)$$

Integrating this expression yields

$$|\delta\mathbf{v}_\perp| \simeq \frac{Gm}{b^2} \int_{-\infty}^{\infty} \left( 1 + \left( \frac{vt}{b} \right)^2 \right)^{-3/2} dt = \frac{2Gm}{bv}. \quad (3.2)$$

The surface density of stars is of order  $N/\pi R^2$  with  $R$  the galaxy's characteristic radius. Per crossing of the galaxy the star thus suffers

$$\delta n = \frac{N}{\pi R^2} 2\pi b db = \frac{2N}{R^2} b db \quad (3.3)$$

encounters in the range  $b$  to  $b + db$ . Each of these encounters induces a perturbation in the test star but because the perturbations caused by the individual encounters are randomly oriented their mean value is zero. Instead the squares of the velocities are added:

$$\delta v_\perp^2 \simeq \left( \frac{2Gm}{bv} \right)^2 \frac{2N}{R^2} b db. \quad (3.4)$$

To find the total change in  $v_{\perp}^2$  this expression is integrated over all possible impact parameters. The largest possible value ( $b_{max}$ ) is the size of the system  $R$  and the smallest possible value ( $b_{min}$ ) occurs when the straight-line approximation breaks down (when  $|\delta\mathbf{v}| \simeq v$ ). We can thus define the minimum impact parameter  $b_{min} \equiv Gm/v^2$ . This leads to

$$\Delta v_{\perp}^2 \equiv \int_{b_{min}}^{b_{max}} \delta v_{\perp}^2 \simeq 8N \left( \frac{Gm}{Rv} \right)^2 \ln \Lambda, \quad (3.5)$$

with  $\ln \Lambda \equiv \ln(b_{max}/b_{min})$ . This is known as the Coulomb logarithm. The typical velocity scale  $v$  of a star can be shown to be

$$v^2 \equiv \frac{GNm}{R}, \quad (3.6)$$

from the virial equations (see Section 3.1.5). This gives

$$\frac{\Delta v_{\perp}^2}{v^2} = \frac{8 \ln \Lambda}{N} \quad (3.7)$$

per crossing. The number of crossings required to change  $v_{\perp}^2$  by order of itself is thus

$$n_r = \frac{N}{8 \ln \Lambda}. \quad (3.8)$$

Now using the expressions for  $\Lambda$ ,  $b_{min}$  and  $v^2$  one finds  $\Lambda \equiv N$ . The relaxation time is defined as

$$t_r = n_r \times t_c. \quad (3.9)$$

Thus systems with ages less than order  $0.1N/\ln N$  crossing times old can be considered collisionless, for example galaxies, otherwise they are collisional, for example star clusters. When a system is collisional it is desirable to avoid softening as close encounters become important.

A more detailed analysis using the Fokker-Planck approximation of Kinetic Theory can be found in chapter 8 of Binney & Tremaine (1987) and gives

$$t_r = \frac{0.34\sigma^3}{G^2 m \rho \ln \Lambda} = \frac{1.8 \times 10^{10} \text{yr}}{\ln \Lambda} \left( \frac{\sigma}{10 \text{km/s}} \right)^3 \left( \frac{M_{\odot}}{\bar{m}} \right) \left( \frac{10^3 M_{\odot} \text{pc}^{-3}}{\rho} \right), \quad (3.10)$$

where  $\sigma$  is the velocity dispersion and  $\rho$  the density. In further discussions this is the relaxation time that I have assumed.

### 3.1.2 Half-mass relaxation time

The relaxation time usually varies between regions in a stellar system. To characterise a system by a single relaxation time which is independent of the density profile, the half-mass relaxation time is useful. This is defined as (Spitzer 1987)

$$t_{rh} = 0.138 \left( \frac{Nr_h^3}{Gm} \right)^{1/2} \frac{1}{\ln(\gamma N)}, \quad (3.11)$$

where  $r_h$  is the half-mass radius and  $\Lambda = \gamma N$  is again the argument of the Coulomb logarithm. Historically the value for  $\gamma$  is 0.4 (Spitzer 1987) and this is the value I will use in my analysis.

### 3.1.3 Core radius

An important global quantity of a stellar system is its core radius. Observationally this is defined as the radius at which the surface brightness drops to half its central value (King 1962). In theoretical work the core radius refers to the natural length-scale of the system, for example King (1966). Casertano & Hut (1985) propose an operational definition of the core radius,  $r_c$ . This has been slightly modified by Aarseth (2001) to obtain a convergent result using a smaller central sample ( $n \simeq N/2$ ),

$$r_c = \left( \frac{\sum_{i=1}^n |\mathbf{r}_i - \mathbf{r}_d|^2 \rho_i^2}{\sum \rho_i^2} \right)^{1/2}, \quad (3.12)$$

where  $\mathbf{r}_i$  are the positions of the individual stars and  $\mathbf{r}_d$  are the coordinates of the density centre,

$$\mathbf{r}_d = \frac{\sum_{i=1}^N \rho_i \mathbf{r}_i}{\sum_{i=1}^N \rho_i}. \quad (3.13)$$

The density estimator  $\rho_i$  is a measure of the local density around a star with at position  $\mathbf{r}_i$  obtained by including the sixth nearest neighbours giving

$$\rho_i = \sum_{j=1}^5 m_j / r_6^3, \quad (3.14)$$

where  $r_6$  is the distance to the the sixth nearest neighbour (Casertano & Hut 1985; Aarseth 2001). This is thus fundamentally different from the core radius used by observers and theoreticians. In the rest of the thesis this operational or density weighted definition is the core radius that is being referred to.

### 3.1.4 Tidal radius

The tidal radius is the outer limit of the cluster. Observationally it is defined as the radius at which the surface brightness reaches zero. It is an extrapolation of the density profile and thus depends on the model used to fit the data.

Theoretically the tidal cut-off radius  $r_t$  is associated with an external gravitational tidal field. If a star moves beyond some critical distance from the cluster centre it is possible for this star to escape the cluster. In a simple approximation where the galaxy is regarded as a point mass and galactic and cluster centres are fixed relative to each other, a star on the line joining the centres of the galaxy and the cluster experiences a tidal force per unit mass

$$F_t = \frac{2rGM_G}{R_G^3}, \quad (3.15)$$

where  $r$  is the distance of the star from the cluster centre,  $M_G$  is the mass of the galaxy and  $R_G$  is the distance between the galactic centre and the centre of the cluster. This will be equal and opposite to the gravitational force from the centre of the cluster at  $r = r_t$ , giving

$$r_t^3 = \frac{M_C}{2M_G} R_G^3, \quad (3.16)$$

with  $M_C$  the cluster mass (von Hoerner 1957). A star moving radially along the line joining the centres can escape the system if it reaches a distance greater than  $r_t$ . Or equivalently when its energy exceeds  $\phi(r_t)$ .

A more elaborate analysis assuming that the cluster is in a circular orbit around the galaxy yields

$$r_t^3 = \frac{1}{3} \frac{M_C}{M_G} R_G^3, \quad (3.17)$$

reducing the tidal radius by a factor 0.87 times the value obtained in equation 3.16 (Spitzer 1987). This result is only exact for stars on the line joining the centres of the cluster and the galaxy. In any other direction the tidal radius is smaller than this. With a value of 2/3 times that of equation 3.17 it is smallest in the direction perpendicular to the joining line.

An approximation for eccentric orbits is the King tidal radius (King 1962).

$$r_t^3 = \frac{1}{3+e} \frac{M_C}{M_G} R_P^3, \quad (3.18)$$

with  $e$  the eccentricity of the cluster orbit and  $R_P$  its distance at perigalacticon. The potential is now time-dependent which prevents an exact determination. Setting  $e = 0$  and  $R_P = R_G$  this is in agreement with equation ??.

### 3.1.5 Collisionless systems and the virial theorem

In a collisionless system at any time  $t$  the full description of its state is given by the distribution function  $f(\mathbf{x}, \mathbf{v}, t)d^3\mathbf{x}d^3\mathbf{v}$ . It specifies the number of stars having positions in the volume  $d^3\mathbf{x}$  centred on  $\mathbf{x}$  with velocities in  $d^3\mathbf{v}$  centred on  $\mathbf{v}$ . It has the characteristic that its flow through phase-space is incompressible. This is described by the *collisionless Boltzmann equation*

$$\frac{df}{dt} = \frac{\partial f}{\partial t} + \mathbf{v} \cdot \nabla f - \nabla \Phi \cdot \frac{\partial f}{\partial \mathbf{v}} = 0. \quad (3.19)$$

From the collisionless Boltzmann equation the scalar virial theorem can be obtained. (For a full derivations see Binney & Tremaine (1987).

$$2K + W = 0, \quad (3.20)$$

leading to

$$\langle v^2 \rangle = \frac{|W|}{M} \quad (3.21)$$

### 3.1.6 Heat capacity in self-gravitating systems and the gravothermal catastrophe

The temperature of a self-gravitating system can in analogy with the ideal gas be defined as

$$\frac{1}{2}m\overline{v^2} = \frac{3}{2}k_B T, \quad (3.22)$$

where  $m$  is the stellar mass and  $k_B$  Boltzmann's constant. The temperature and rms velocity generally depend on position and thus

$$\overline{T} = \frac{\int \rho(\mathbf{x})T d\mathbf{x}}{\int \rho \mathbf{x} d\mathbf{x}}. \quad (3.23)$$

The total kinetic energy

$$K = \frac{3}{2}Nk_B\overline{T} \quad (3.24)$$

and from the virial theorem (see Section 3.1.5) this is related to the total energy

$$E = -K. \quad (3.25)$$

The heat capacity is

$$C \equiv \frac{dE}{d\overline{T}} = -\frac{3}{2}Nk_B \quad (3.26)$$

and is *negative*. This means that by adding energy to the system it cools. This might be counter-intuitive but is nevertheless true for all systems that

are dominated by gravitational forces. This means that once a system that is in contact with a heat bath transfers a little amount of heat to the heat bath, it will heat up and more heat will flow into the heat bath and consequently the system will heat up even more. This cycle will continue and the temperature will rise without limit. Similarly, if heat is added to the system, it will cool till the temperature reaches zero. Thus systems with negative heat capacities are unstable. This is called the gravothermal catastrophe.

## 3.2 Evolution trends in spherical systems

The relaxation time is inversely proportional to the density (equation 3.10). Thus relaxation effects happen first in the core of the cluster where the density is highest. In the halo encounters have little effect, but over time the halo is augmented by stars that were originally in the core but have gained energies close to the escape energy owing to encounters. After a few core relaxation times these stars will overwhelm original halo members. There are a number of physical processes that influence the evolution of a globular cluster. They are individually described below. But they occur simultaneously and it might be hard to distinguish between different processes in practice.

### 3.2.1 Evaporation and Ejection

There are two distinctly different ways in which stars can escape from a cluster. The first is called ejection and refers to a process where a star is removed by a single close encounter with another star in which one star gains enough velocity to exceed the local escape speed. The second is called evaporation and this is escape of a star resulting from a series of more distant encounters, gradually increasing its energy. This process is more complicated. A series of weak encounters cause a star to random-walk through phase-space. Energetic stars with highly elongated orbits will experience a significant number of encounters when they pass through the core and they might wander into a portion of phase-space associated with unbound orbits. Galactic tidal forces can substantially increase the evaporation rate. The ejection and evaporation time are defined as

$$t_{ej} = 1.1 \times 10^3 \ln(0.4N)t_{rh}, \quad (3.27)$$

$$t_{ev} = 300t_{rh}. \quad (3.28)$$

In most cases  $t_{ej} \gg t_{evap}$  so ejection can mostly be neglected compared to evaporation.

### 3.2.2 Core collapse

As could be seen in figure 2.3 the radius containing 90% of the mass fraction expands with time while the radius containing 10% of the mass decreases. This process is known as core collapse. It is a two-stage process. Encounters in the core drive stars out to the halo (evaporation) and by energy conservation laws the core must shrink. In the second stage the rate of core collapse appears to accelerate. This is suspected to be the result of the gravothermal catastrophe described in section 3.1.6. The inner parts of the system have negative heat capacity. Thus the loss of energy results in heating the system. There is thus a negative temperature (i.e. velocity dispersion) gradient outward, causing the centre to continually lose energy, shrink, and heat up.

If these results are extrapolated one would eventually expect a singularity to occur in the centre. However before this happens binary formation kicks in which prevents this singularity from forming. This process will be described in section 3.2.4.

### 3.2.3 Equipartition

In a (more realistic) system that contains stars of different masses encounters tend to establish equipartition of kinetic energy. More massive stars lose their energy and sink to the centre while lighter stars tend to gain energy and their orbits expand. This is called mass segregation. Equipartition appears to occur on time scales comparable to the  $t_{rh}$ .

For a system containing two populations of stellar masses  $m_1$  and  $m_2$ , with  $m_2 \gg m_1$ , it can be shown (Binney & Tremaine 1987) that the criterion for equipartition is

$$\frac{M_2}{\rho_{c1} r_{c1}^3} \lesssim 4 \left( \frac{m_1}{m_2} \right)^{3/2} \quad (3.29)$$

where  $M_2$  is the total mass of the heavy stars,  $\rho_{c1}$  and  $r_{c1}$  are the central density and King radius (cf. Equation 3.18) of the light population. If the total mass of the heavy stars is too large they form an independent self-gravitating system. Encounters cause the heavy stars to lose energy to the light stars, increasing their own velocity dispersion, losing energy, shrinking, heating up and thus moving away from equipartition. This is called the equipartition instability.

### 3.2.4 Binary formation

When a system is no longer collisionless close encounters between stars can raise tides that dissipate their relative orbital kinetic energy. This loss may

be so large that the stars form a binary. Two types of binaries can be distinguished. Those with a small binding energy are called soft and those with a large binding energy are called hard. Soft binaries are generally short lived and unimportant in the evolution of a stellar system. However hard binaries have a profound effect on core collapse (Ostriker 1985). When hard binaries encounter another field star they interact in an extremely complex manner in which the field star can become bound to the system temporarily forming a triple system. Finally one of the three stars will be ejected from the system with a higher speed than the originally incoming star. From conservation of energy it thus follows that the potential energy of the binary system (which is negative) decreases and it will thus become more tightly bound.<sup>1</sup> Energy released by the binary will be shared with other cluster members through encounters. The binary thus acts as an energy source in the core thus halting core collapse.

---

<sup>1</sup>This phenomenon is half of Heggie's law: *hard binaries get harder and soft binaries get softer*

# Chapter 4

## nbody6

The basic code used in Chapter 2 is generally known as `nbody1`. Since then the code has developed and I will briefly discuss the main extensions and improvements that have led to `nbody6`. The descriptions in the next three sections borrow heavily from Aarseth (2003)

### 4.1 Hermite integration

As technology advanced over the years special purpose hardware was developed to produce very fast force and force derivative calculations which were subsequently returned to the main program. A new integration scheme was introduced replacing the standard polynomial scheme described in Section 2.1. It increased the accuracy of the integration by using the explicit values for the force and its derivative to include a high order corrector. This is achieved by expanding the force and its first derivative in a Taylor series about the reference time  $t$  as

$$\mathbf{F} = \mathbf{F}_0 + \mathbf{F}_0^{(1)}t + \frac{1}{2}\mathbf{F}_0^{(2)}t^2 + \frac{1}{6}\mathbf{F}_0^{(3)}t^3, \quad (4.1)$$

$$\mathbf{F}^{(1)} = \mathbf{F}_0^{(1)} + \mathbf{F}_0^{(2)}t + \frac{1}{2}\mathbf{F}_0^{(3)}t^2. \quad (4.2)$$

From this  $\mathbf{F}_0^{(3)}$  and  $\mathbf{F}_0^{(2)}$  can be written as

$$\mathbf{F}_0^{(3)} = \left( 2(\mathbf{F}_0 - \mathbf{F}) + \left( \mathbf{F}_0^{(1)} + \mathbf{F}^{(1)} \right) t \right) \frac{6}{t^3}, \quad (4.3)$$

$$\mathbf{F}_0^{(2)} = \left( -3(\mathbf{F}_0 - \mathbf{F}) - \left( 2\mathbf{F}_0^{(1)} + \mathbf{F}^{(1)} \right) t \right) \frac{2}{t^2}. \quad (4.4)$$

These can now be used to apply a third order corrector to the position and velocity coordinates

$$\Delta \mathbf{r}_i = \frac{1}{24} \mathbf{F}_0^{(2)} \Delta t^4 + \frac{1}{120} \mathbf{F}_0^{(3)} \Delta t^5, \quad (4.5)$$

$$\Delta \mathbf{v}_i = \frac{1}{6} \mathbf{F}_0^{(2)} \Delta t^3 + \frac{1}{24} \mathbf{F}_0^{(3)} \Delta t^4. \quad (4.6)$$

## 4.2 Time-steps

### 4.2.1 Improved time-step criterion

The time-step described by Equation 2.7 is redefined (Aarseth 1985) as

$$\Delta t_i = \left( \frac{\eta(|\mathbf{F}| |\mathbf{F}^{(2)}| + |\mathbf{F}^{(1)}|^2)}{(|\mathbf{F}^{(1)}| |\mathbf{F}^{(3)}| + |\mathbf{F}^{(2)}|^2)} \right)^{1/2}. \quad (4.7)$$

Now all force derivatives play a role and it is also well-defined for special cases, for example when one of the components tends to zero.

### 4.2.2 Block time-steps

The prediction overhead introduced by the Hermite scheme can be reduced by grouping particles and advancing them simultaneously. Hierarchical levels are defined (in standard units) as

$$\Delta t_n = \frac{1}{2^{n-1}}. \quad (4.8)$$

The time-step is now selected to be the nearest truncated value of the natural time-step defined in Equation 4.7. The time-steps initially defined by Equation 4.8 may be reduced or increased by a factor 2 every now and then if subsequent time-steps start to differ too much.

An advantage of the Hermite scheme is that it is self-starting. No initial time-steps have to be specified. Also the polynomials do not require evaluation of the second and third order force derivative as in Equation 2.6 making the corrector significantly faster.

## 4.3 Other important additions

### 4.3.1 Binary formation and hierarchical systems

In a real stellar system close encounters occur and this can lead to binary formation. In early versions of  $N$ -body programs this problem was circumvented

by introducing a softening parameter to prevent such close encounters. However binaries have a profound effect on the evolution of a cluster as described in Section 3.2.4. When two particles get close together time-steps become very small resulting in large computation times. Methods have been developed for dealing with this and `nbody6` has the Kustaanheimo-Stiefel (called KS-regularization, Kustaanheimo & Stiefel 1965) method implemented. If two particles get very close together they are treated by integrating their centre of mass as a single particle together with its relative motion. This is generally more efficient than integrating the two particles separately. For a complete description of the method and its implementation see Aarseth (2003).

Sometimes higher order systems form when binaries interact with other stars or even other binaries. This is treated in a similar way where the system is treated as two or more simultaneous KS regularisations. For a detailed description see Aarseth & Zare (1974)

### 4.3.2 Neighbour scheme

In order to increase efficiency the evaluation of the force contributions from distant particles is reduced by splitting the total force on a particle into an irregular and a regular component. The force summation is now only carried out over the nearest particles while the contribution from the more distant particles is predicted assuming it is smoothly varying. This is called the Ahmad and Cohen or AC neighbour scheme (Ahmad & Cohen 1973).

### 4.3.3 Stellar evolution

In a real stellar cluster stars evolve over their lifetime and consequently lose mass. This effects the relative forces between particles and should thus be taken into consideration. In `nbody6` stellar evolution is treated based on fast look-up functions which provide information on the stellar type, radius and mass for a given initial mass, age and metallicity (Tout et al. 1997; Hurley et al. 2000). Mass loss correction can thus be accounted for. Neutron stars resulting from a supernova are assigned a kick velocity and generally disappear from the cluster.

### 4.3.4 External tidal fields

There are options in `nbody6` to include an external galactic tidal field. The first option defines the standard case based on the local Oort constants and is thus special for our own position in the Milky Way at 8.5 kpc from the

galactic centre. Another option lets you specify the orbital distance of the cluster and the galactic mass which is then treated as a central point source. A more realistic case can be treated with the third option which consists of three components: a bulge (again a point mass), a disk, and a logarithmic potential. The disk is treated as a Miyamoto-Nagai disk (Miyamoto & Nagai 1975) and is governed by three parameters: its mass and its horizontal and vertical scale lengths. The logarithmic potential describes the halo.

## 4.4 Hardware

Simulations were carried out on the supercomputer at Swinburne called "The Green Machine" (due to its increased performance-per-Watt over previous processors). It comprises 145 Dell Power Edge 1950 nodes each with 2 quad-core Clovertown processors at 2.33 GHz. Each processor is 64-bit low-volt Intel Xeon 5138. The nodes have 16 GB of RAM and two 500 GB drives each.

The  $N$ -body problem goes as  $N^3$ . There are  $N^2$  force calculations and a cluster's life time increases roughly linearly with the cluster size (cf. eq. 3.11). Hence increasing the system size will increase the CPU time dramatically. In order to keep computing times low the stellar systems I have studied are not full size globular clusters but systems with  $N = 1000$ .

As mentioned before in recent years special purpose computers have been developed to carry out the force and its derivative calculations. `nbody4` was developed for the HARP computer (Hermite AcceleratoR Pipe) and was subsequently adjusted for workstations and supercomputers as `nbody6` thus employing the Hermite scheme but still calculating the force and derivative internally.

## 4.5 Input file and user options

The code expects an input file in which the user should specify input parameters and options. After a line of `nbody6` control parameters there are six lines starting with two defining the cluster properties (e.g.  $N$ , maximum neighbour number, total mass, virial radius) and accuracy and decision-making parameters (e.g. time-steps, energy tolerance, output intervals). These lines are followed by 40 options. These control a variety of parameters, the most important ones I have described in the sections above. Then there is a line controlling the KS regularization followed by one specifying the IMF parameters. The last line is the virial theorem scaling. Most of the accuracy

parameters do not need any adjustment. The most important options for me are the cluster properties, stellar evolution scheme and external field. When specifying a none-standard tidal field, an extra line needs to be added, specifying the different components (i.e. mass, scale lengths).

## 4.6 Other methods

There are alternative ways in which one can model the evolution of stellar systems. For example there is the Fokker-Planck method which is based on the collisionless Boltzmann equation described in Section 3.1.5. However as the name suggests this formulation breaks down after the system becomes relaxed and is no longer collisionless.

# Chapter 5

## Results using existing options

### 5.1 Simulations with nbody6

I first ran a set of models to study the effects of IMF, stellar evolution and the addition of the standard tidal field on the evolution of the cluster. They are listed in table 5.1. All models start with 1000 single stars distributed according to the Plummer model (see Section 2.3) and no primordial binaries. One of the differences between them is the mass spectrum used. In a model either all stars have the same mass ( $1M_{\odot}$ ) or they are distributed according to a Salpeter IMF ( $n(M) \propto M^{-2.3}$ ) with a minimum and maximum stellar mass  $m_{min} = 0.3M_{\odot}$  and  $m_{max} = 30M_{\odot}$  respectively. The total stellar mass is  $1000M_{\odot}$ . Also a model has either no stellar evolution at all or stellar evolution according to the mass loss scheme by Hurley et al. (2000) explained in section 4.3.3. The third difference is the presence of an external tidal field. A cluster is either isolated in space or experiences a standard external Galactic tidal

Model nr.	IMF	Stellar evolution	Tidal field
1	·	·	·
2	+	·	·
3	+	+	·
4	·	·	+
5	+	·	+
6	+	+	+

Table 5.1: Overview of the models used in my simulations. All models have  $N = 1000$ .

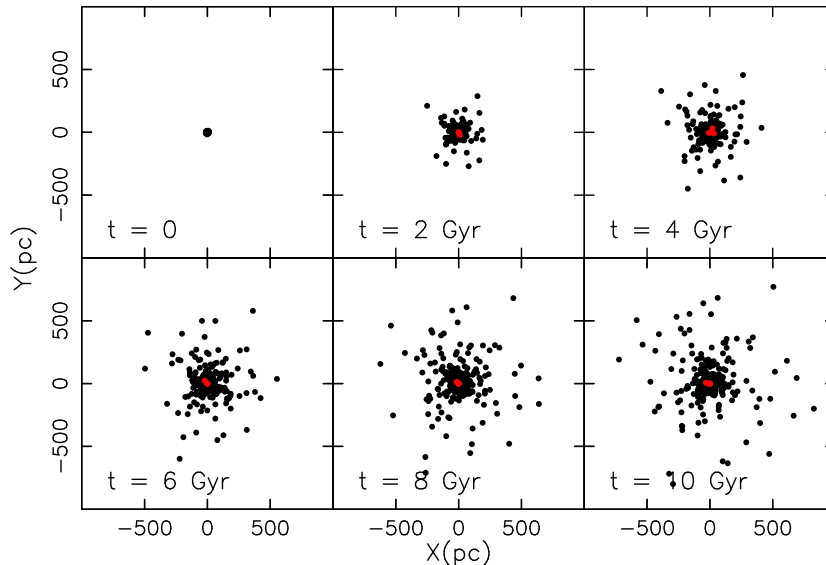


Figure 5.1: Projected spatial distribution: Model 1. Black dots are single stars. Red dots are binaries.

field which is represented by a point mass 8.5 kpc away (the distance from our sun to the Galactic centre). Model 1 is the most basic model: an isolated cluster of equal mass stars that undergo no stellar evolution. It is the same as the model used in Chapter 2. Subsequent models introduce a mass spectrum, stellar evolution and a standard tidal field.

### 5.1.1 Results using `nbody6`

The first model is chosen to resemble the model from the sample simulation with `nbody1` from Chapter 2. Its spatial evolution is shown in figure 5.1 and 5.2. Comparing these to the sample simulation (Figures 2.1 and 2.2) the same general expansion can be seen. In `nbody6` the cluster size is limited by a tidal radius. For an isolated cluster this means that evaporating stars that have moved too far away are no longer considered part of the cluster. The tidal radius is set to be 10 times the scale length  $r_s$  which is defined as

$$r_s = \frac{1}{2} \frac{M_{tot}^2}{\Phi} \quad (5.1)$$

with  $M_{tot}$  the total cluster mass and  $\Phi$  the potential energy. The collapsing core that was evident in the sample simulation is not so obvious in this model. One of the main differences between the sample code and `nbody6` is

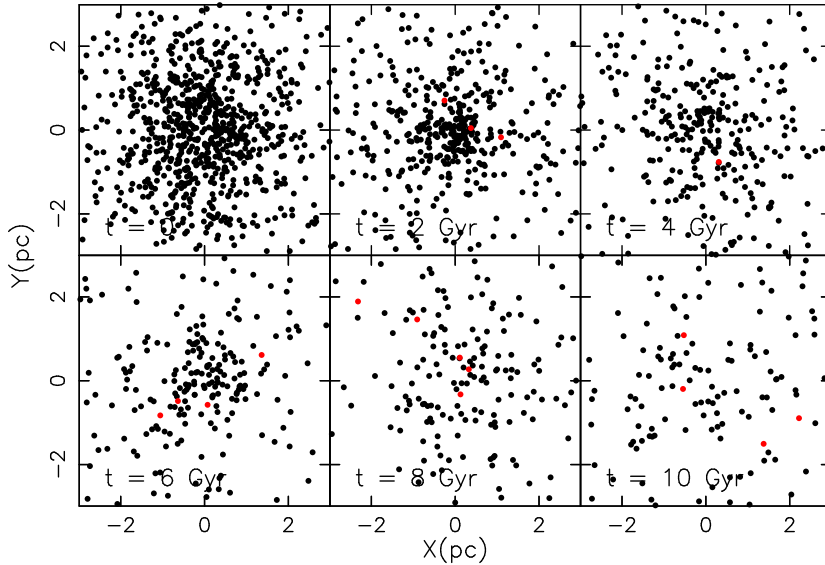


Figure 5.2: Projected spatial distribution in the core: Model 1. Labels as in figure 5.1

the ability to deal with close encounters. This problem was avoided before by introducing a softening parameter. In `nbody6` binaries can form and the energy gain that caused the core to collapse in the sample simulation is now stored in the binding energy of the binary systems that formed in the core as a result of close encounters (see Section 3.2.4). In this model the first binary formed after roughly 450 Myrs and at the time the simulation ended (after 10 Gyrs) it has 6 hard binaries. The evolution of the density distribution is shown in Figure 5.3 and can be compared to Figure 2.5. The same behaviour is visible. Again starting from a Plummer model the density in the core initially increases but decreases later as binaries form.

Model 2 introduces the mass spectrum. The effects of this on the total mass loss can be seen in Figure 5.4. While in model 1 the rate of star loss is roughly continuous, introduction of a mass spectrum causes the system to lose more stars early on. This can be contributed to mass segregation. Lighter stars gain kinetic energy through equipartition during encounters with heavy stars in the core and are more likely to escape. In this particular run there is a sudden loss of mass at about 3.4 Gyr. This is due to an escaping hierarchical system consisting of massive stars. Also shown is Model 3 which adds stellar evolution leading to the loss of even more stars in the early stages. Heavy stars evolve fast and hence lose mass quickly. Neutron stars that form from a supernova will get a velocity kick and generally disappear

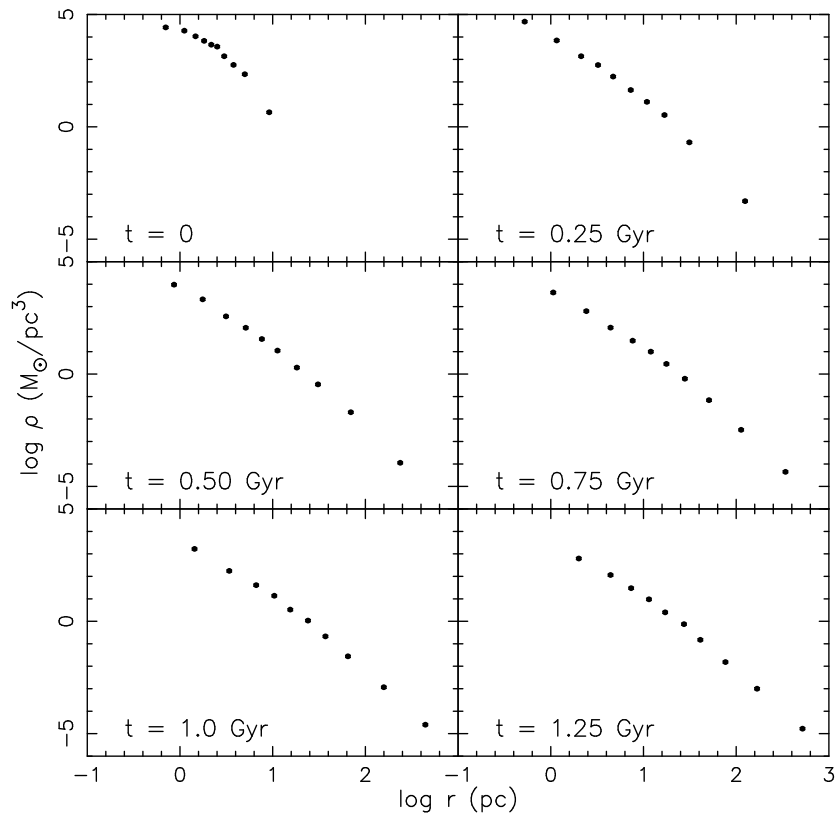


Figure 5.3: The density distribution evolution for Model 1. The data is binned in ten equally sized bins.

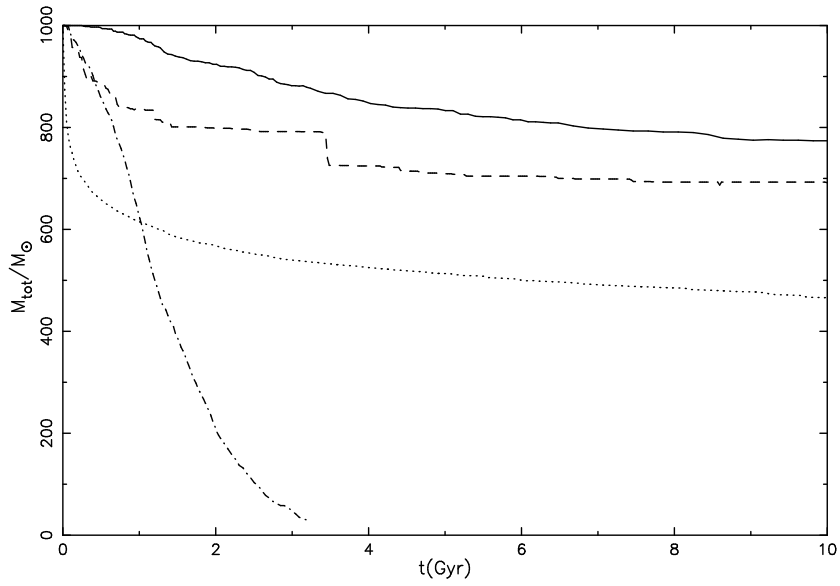


Figure 5.4: The evolution of the total mass of the cluster for Model 1 (solid), Model 2 (dashed), Model 3 (dotted) and Model 4 (dash-dotted)

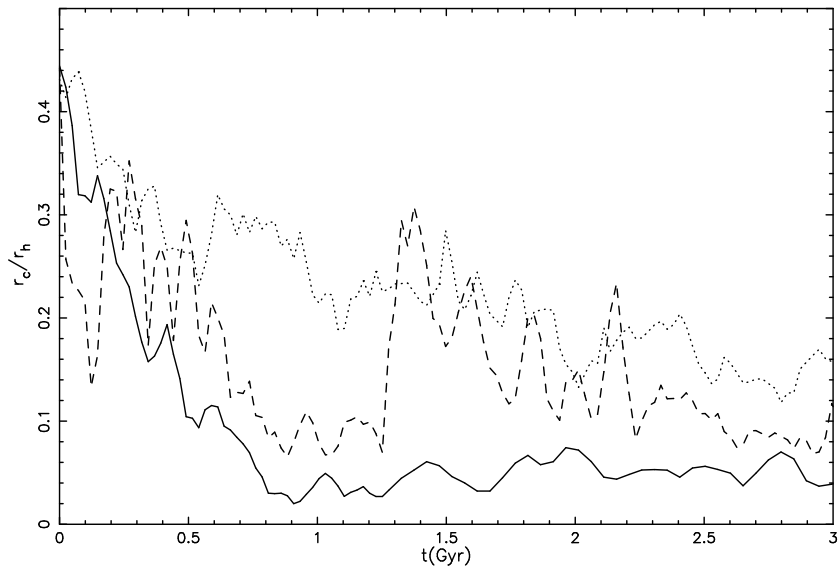


Figure 5.5: The ratio of core radius to half mass radius for models 1, 2 and 3. The curves are smoothed by averaging over three time bins. Labels as in Fig 5.4

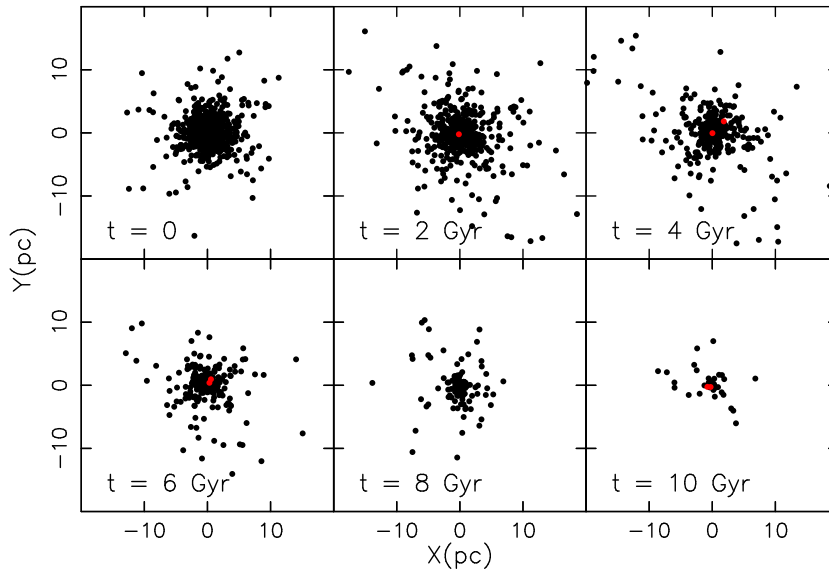


Figure 5.6: Projected spatial distribution: model 4

from the system.

Figure 5.5 also shows core collapse. The ratio of core radius to half mass radius decreases over time for all three models. When introducing an IMF a rapid (but noisy) core collapse is visible initially owing to mass segregation. When stellar evolution is added as well the core initially expands due to the heaviest stars losing mass quickly and the ejection of neutron stars. The overall collapse is also shallower because of the expansion of the system as a whole due to mass loss.

Models 4, 5 and 6 correspond to Models 1, 2 and 3 respectively but this time the external tidal field is turned on. This field will strip stars of the cluster and simulations are stopped when the cluster has only 25 or less stars left. For Model 4 this is after about 3 Gyr. Figure 5.6 shows the spatial evolution of the cluster over its lifetime. How much influence the tidal field has on the mass loss can be seen by comparing it to the evolution of the mass of Model 1 (Figure 5.4). An almost constant very high mass loss rate dissolves the cluster quickly in the presence of a tidal field. Also the density distribution is shown in Figure 5.7. Compared to Model 1 the overall density decreases faster. More so in the outer regions where most stars will be stripped off. Because the tidal radius is actually defined here as the King tidal radius (cf. Equation 3.17) it is a lot smaller than the the tidal radius used for Model 1 as can be seen in the figure as well. Towards the end of the life time of the cluster this data becomes noisy because there are

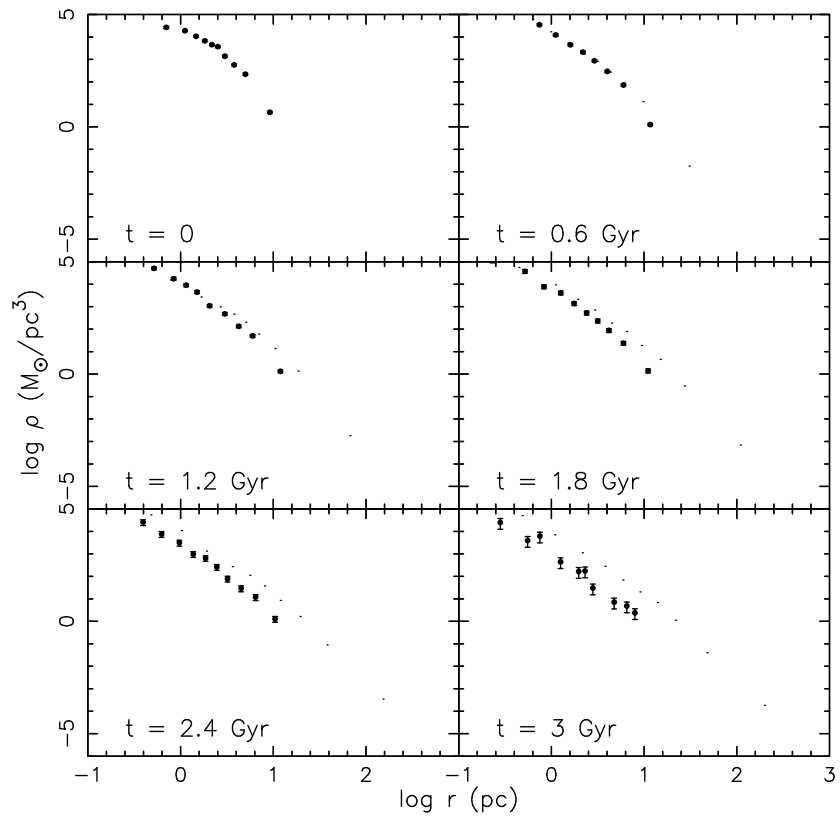


Figure 5.7: The density distribution evolution of Model 4. For comparison Model 1 is plotted as the small dots.

only a few data points left in each bin. Figure 5.8 compares core collapse for Model 1 and 4. As can be seen the addition of a tidal field does not influence core collapse. At later stages the tidal field keeps stripping stars of the outer regions thus decreasing the half-mass radius. This is consistent with results from Giersz & Heggie (1997) who show that core collapse is almost unaffected by the tide.

Figure 5.9 shows the density distribution for Model 6 until its disruption at 1.25 Gyrs. Compared to Model 4 (in Figure 5.7) the initial core density drops fast owing to stellar evolution and mass segregation while in the outer regions the same behaviour is seen. Overall the cluster disrupts faster because both stellar evolution and the tidal field lead to increased mass loss. Core collapse behaves very differently for Models 4, 5 and 6 as is shown in Figure 5.10. As already shown in Figure 5.8 the addition of just a tidal field does not have an influence on core collapse. However adding an IMF drives early core collapse (as in Model 2) but combined with the addition of the tidal field this results in a fast decrease of the half-mass radius and earlier dissolution. Adding stellar evolution again delays core collapse. For an isolated cluster the half-mass relaxation time generally increases with time. Almost no stars are lost from the cluster so the half-mass relaxation time only depends on the half-mass radius (cf. Equation 3.11) which slowly increases with time. Adding a tidal field means reducing  $N$  dramatically which will also reduce  $t_{rh}$ . Adding an IMF however means mass segregation and earlier collapse driving out the half-mass radius, thus increasing the relaxation time initially and then rapidly decreasing as  $N$  drops. Adding stellar evolution shows a similar trend but less extreme due to the delay in core collapse.

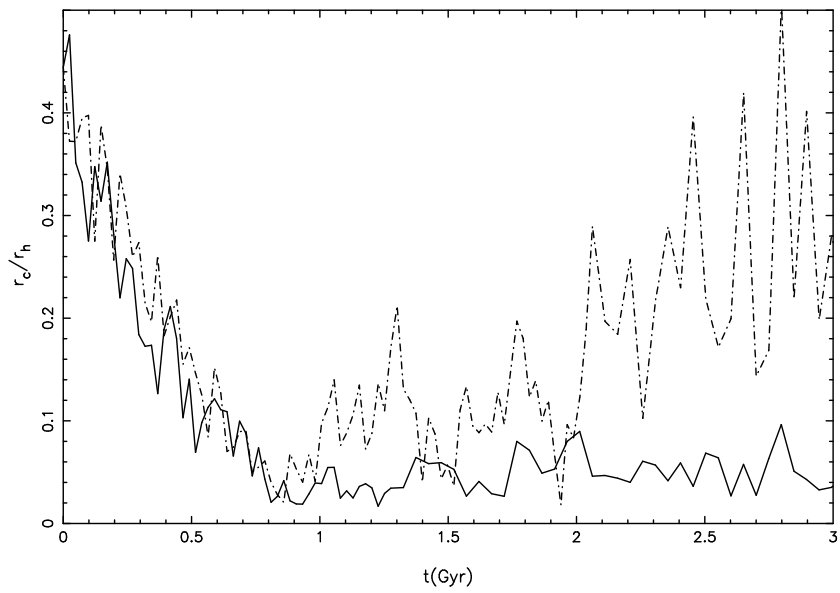


Figure 5.8: The core radius to half mass radius for Model 1 (solid) and 4 (dash-dotted). This time the data has not been smoothed.

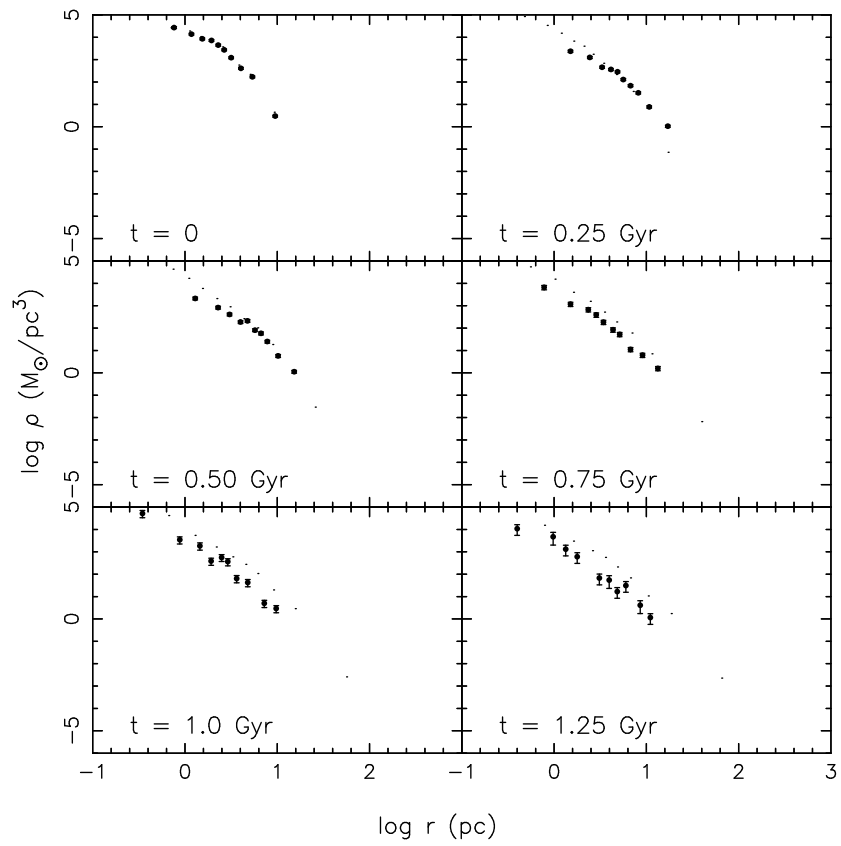


Figure 5.9: The density distribution evolution of Model 6. For comparison Model 1 is plotted as the small dots.

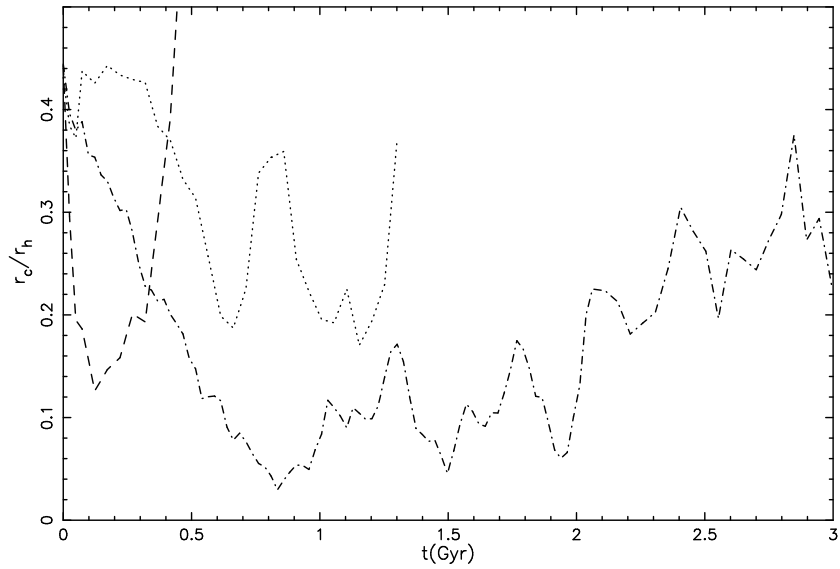


Figure 5.10: The core radius to half mass radius for Model 4 (dashed-dotted), 5 (dashed) and 6 (dotted) smoothed over three data bins.

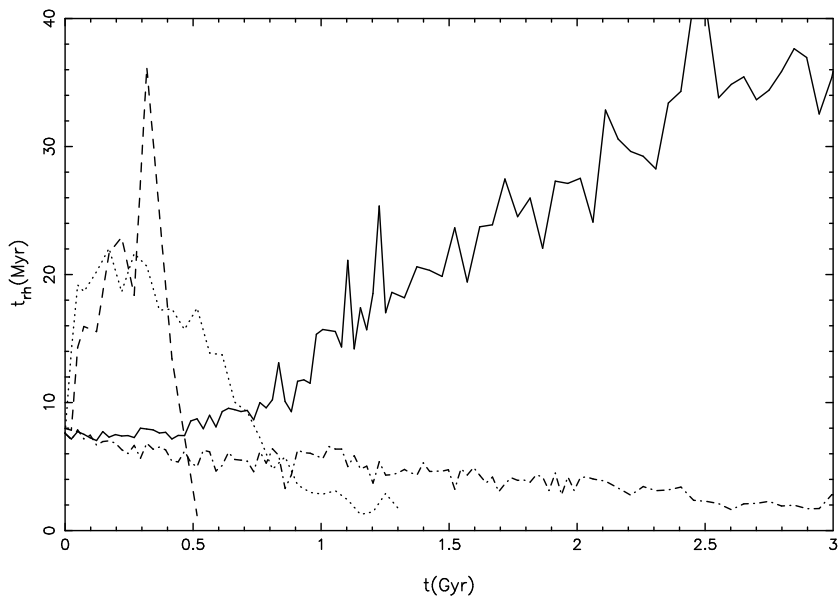


Figure 5.11: The half-mass relaxation time for Models 4, 5 and 6. Legend as in Figure 5.10. Also shown is Model 1 (solid).

# Chapter 6

## Including a nfw dark matter halo

### 6.1 The Navarro, Frenk and White density profile

$N$ -body simulations of dark matter halos show that they can be described by the same scaled density profile over a large range in mass from galaxies to galaxy clusters (Navarro et al. 1996)

$$\frac{\rho(r)}{\rho_{crit}} = \frac{\delta_c}{r/r_s(1+r/r_s)^2}, \quad (6.1)$$

where  $\rho_{crit}$  is the critical density  $3H^2/8\pi G$  at redshift  $z = 0$  required for a flat universe. In this  $H$  is the Hubble parameter and  $\delta_c$  the characteristic overdensity related to the concentration parameter  $c$  through

$$\delta_c = \frac{\Delta_{vir}}{3} \frac{c^3}{\ln(1+c) - c/(1+c)}. \quad (6.2)$$

and normalises the profile so that the integration over the volume of the halo gives the virial mass

$$M_{vir} = \frac{4\pi}{3} \Delta_{vir} \rho_{crit} r_{vir}^3; \quad (6.3)$$

The concentration parameter  $c$  relates to the scale radius  $r_s$  to the virial radius  $r_{vir}$  as  $c = r_{vir}/r_s$ . The virial radius is defined as the radius within which the average density is  $\Delta_{vir} \times \rho_{crit}$  where  $\Delta_{vir}$  is the virial overdensity criterion defining the average density as some multiple of the background density. This density profile (generally known as the NFW-profile) behaves

as  $r^{-2}$  around the scale radius thus representing an isothermal sphere but flattens out in the centre toward a  $r^{-1}$  profile. In the outer parts, away from the scale radius it gradually steepens toward a  $r^{-3}$  profile.

## 6.2 Addition of NFW halo to nbody6

To add the possibility of a NFW halo to the code I need the force and the time derivative of the force resulting from this halo. The force is calculated by taking the negative gradient of the potential ( $\mathbf{F} = -\nabla\Phi$ ). The potential associated with the NFW density profile is (Cole & Lacey 1996)

$$\Phi(r) = -\frac{V_{vir}^2}{g(c)} \frac{\ln(1+r/r_s)}{r/r_s}, \quad (6.4)$$

with

$$g(c) = \frac{\ln(1+c)}{c} - \frac{1}{1+c} \quad (6.5)$$

and  $V_{vir}^2 = GM_{vir}/r_{vir}$  is the virial velocity of the halo.

Making the substitution

$$s = r/r_s, \quad ds = dr/r_s,$$

this becomes

$$\Phi(r) = -\frac{V_{vir}^2}{g(c)} \left[ \frac{\ln(1+s)}{s} - \frac{1}{1+c} \right]$$

giving the force

$$\begin{aligned} F(r) &= -\frac{d\Phi}{dr} = -\frac{d\Phi}{ds} \frac{ds}{dr} \\ &= \frac{1}{r_s} \frac{V_{vir}^2}{g(c)} \left[ \frac{s/(1+s) - \ln(1+s)}{s^2} \right] \\ &= \frac{V_{vir}^2}{g(c)r_s} \left[ \frac{1}{s(1+s)} - \frac{\ln(1+s)}{s^2} \right]. \end{aligned} \quad (6.6)$$

$$(6.7)$$

It is spherically symmetric so the  $\theta$  and  $\phi$  components of the gradient are zero.

Now for the time derivative of this force

$$\begin{aligned}
\frac{dF(r)}{dt} &= \frac{dF}{ds} \frac{ds}{dt} \\
&= \frac{V_{vir}^2}{g(c)r_s} \left[ -\frac{1}{s(1+s)^2} - \frac{1}{s^2(1+s)} - \frac{s^2/(1+s) - 2s \ln(1+s)}{s^4} \right] \dot{s} \\
&= -\frac{V_{vir}^2}{g(c)r_s} \left[ \frac{2+3s}{s^2(1+s)^2} - \frac{2 \ln(1+s)}{s^3} \right] \dot{s} \tag{6.8}
\end{aligned}$$

### 6.3 Cartesian coordinates

To incorporate this into the code Cartesian coordinates are needed. If I consider the  $x$  component it follows that

$$\begin{aligned}
F(x) &= -\frac{d\Phi}{dx} = -\frac{d\Phi}{dr} \frac{dr}{dx} = \frac{x}{r} F(r) \\
&= \frac{V_{vir}^2}{g(c)r_s^2} \left[ \frac{1}{s^2(1+s)} - \frac{\ln(1+s)}{s^3} \right] x. \tag{6.9}
\end{aligned}$$

The force derivative is a bit more tedious because the force is now a function of  $s$  and  $r$  and so time derivatives with respect to both coordinates are needed:

$$\begin{aligned}
\frac{dF(x)}{dt} &= \frac{d}{dt} \left( \frac{x}{r} F(r) \right) = \frac{F(r)}{r} \frac{dx}{dt} - \frac{x F(r)}{r^2} \frac{dr}{dt} + \frac{x}{r} \frac{dF(r)}{dt} \\
&= \frac{V_{vir}^2}{g(c)r_s^2} \left[ \frac{1}{s^2(1+s)} - \frac{\ln(1+s)}{s^3} \right] \frac{dx}{dt} \\
&\quad - \frac{V_{vir}^2}{g(c)r_s^3} \left[ \frac{1}{s^3(1+s)} - \frac{\ln(1+s)}{s^4} \right] x \frac{dr}{dt} \\
&\quad - \frac{V_{vir}^2}{g(c)r_s^2} \left[ \frac{2+3s}{s^3(1+s)^2} - \frac{2 \ln(1+s)}{s^4} \right] x \frac{ds}{dt} \\
&= \frac{V_{vir}^2}{g(c)r_s^2} \left[ \frac{1}{s^2(1+s)} - \frac{\ln(1+s)}{s^3} \right] \frac{dx}{dt} \\
&\quad - \frac{V_{vir}^2}{g(c)r_s^4} \left[ \frac{3+4s}{s^4(1+s)^2} - \frac{3 \ln(1+s)}{s^5} \right] x \mathbf{r} \cdot \mathbf{v}_r, \tag{6.10}
\end{aligned}$$

where I have used

$$\frac{dr}{dt} = \frac{1}{r} \left( x \frac{dx}{dt} + y \frac{dy}{dt} + z \frac{dz}{dt} \right) = \frac{\mathbf{r} \cdot \mathbf{v}_r}{r}.$$

Similar expressions hold for the  $y$  and  $z$  components of the force.

Model	Point mass	Disk	NFW halo
I	·	+	·
II	+	+	·
III	·	·	+
IV	+	+	+
V	+	·	+

Table 6.1: Overview of the models used in my simulations. All models have  $N = 1000$ .

## 6.4 Addition to the code

I have written a subroutine `fnfw` that calculates the force and force derivatives resulting from the halo as described in the previous section. This is now incorporated into the code as another galactic component which are mainly managed from the subroutine `xtrn10`. It needs three input parameters which are the virial mass of the halo, the concentration of the halo and the virial overdensity criterion. The result of this inclusion of the option of a NFW halo is that the input file format has slightly changed. Option (#14) is set to three to define a full galactic model. The input line for the parameters for the galactic field is expanded so the user can specify the desired virial mass, concentration and overdensity criterion for the NFW halo.

## 6.5 Experiments

In chapter 5 I showed the influence of a standard galactic tidal field to the evolution of a 1000 star cluster. In this chapter I use the option to 'build-up' my own galaxy that `nbody6` offers. I use three different components: the disk, the bulge and the halo. I have run a set of models for various combinations of these components shown in table 6.1.

### 6.5.1 Adding the disk + bulge

The first thing I did was adding a background galaxy (no dark matter) to the models starting out with just a disk (Model I). I then went on to add a bulge to this as well (Model II). The disk is modeled as a Miyamoto-Nagai disk (Miyamoto & Nagai 1975) and the bulge is just a point mass in the centre of the galaxy. I use a mass of  $5 \times 10^{10} M_{\odot}$  for the disk and  $1.5 \times 10^{10} M_{\odot}$  for the bulge as suggested by Xue et al. (2008).

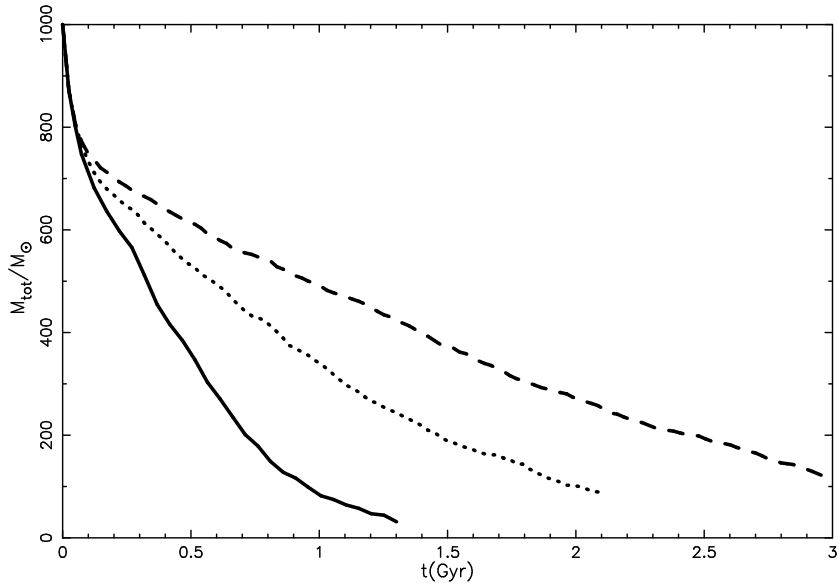


Figure 6.1: The total mass evolution of the cluster in different external conditions. The solid line is when a standard galactic tidal field based on the Oort constants is applied (Model 6 from Chapter 5). The dashed line is when the galaxy is represented by just a Miyamoto-Nagai disk (Model I). The dotted line is a full galactic model including the Miyamoto-Nagai disk and a bulge (Model II).

I adopt a tidal radius roughly equal to King radius (see Equation 3.17) of 16 pc for all the models at an orbital distance of 8.5 kpc (the distance from our sun to the galactic centre. This was kept the same when I put the cluster on different orbits or added a dark matter halo.

Figure 6.1 shows the evolution of the cluster mass for different external tidal fields. My galactic model does not produce a tidal field as strong as the standard field. This already shows that there is a problem with the way the galaxy is modeled with just disk and bulge.

### 6.5.2 The evolution of the cluster in a pure NFW halo

Here I present the results for a set of models in a pure NFW dark matter halo (Model III) using a overdensity criterion  $\Delta_{vir} = 200$ . The halos are then defined by two free parameters. I use a model grid of 6 different halo virial masses ( $10^9 M_\odot, 10^{10} M_\odot, 10^{11} M_\odot, 1.5 \times 10^{12} M_\odot, 10^{13} M_\odot$  and  $10^{14} M_\odot$ ) and 3 concentrations (5, 10 and 15) thus 18 models in total I put the cluster on a

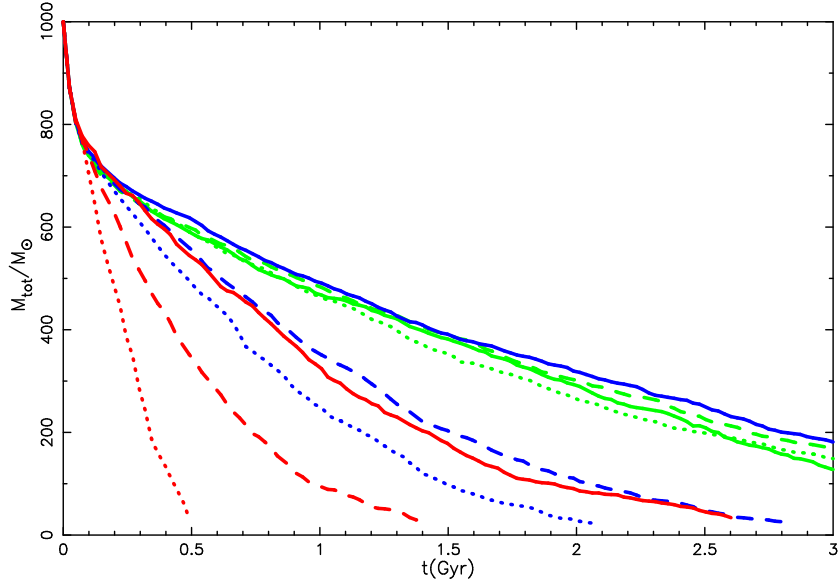


Figure 6.2: The total mass evolution of a cluster of 1000 stars at an orbital distance of 8.5 kpc from the halo centre. I am showing three different virial masses -  $10^9 M_\odot$  (green),  $1.5 \times 10^{12} M_\odot$  (blue) and  $10^{14} M_\odot$  (red) - each with three different concentrations  $c = r_{vir}/r_s - 5$  (solid), 10 (dashed) and 15 (dotted).

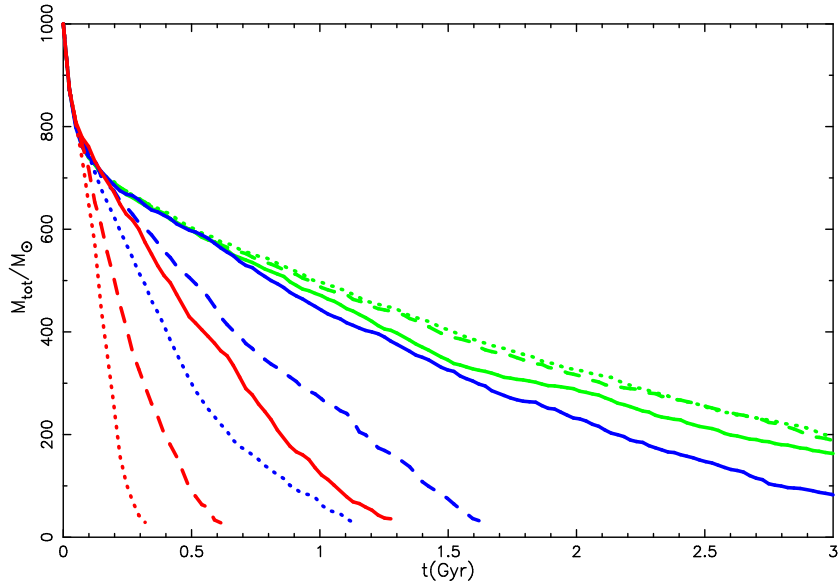


Figure 6.3: The total mass evolution of a cluster of 1000 stars at an orbital distance of 4.5 kpc from the halo centre. Labels as in figure 6.2.

circular orbit at a distance of 8.5 kpc from the centre of the halo. This is achieved by giving the cluster an initial velocity equal to the halo velocity at that distance  $V_c = \sqrt{GM(< r)/r}$ . All subsequent simulations start with 1000 stars with a Salpeter IMF in the mass range  $0.1 - 10.0M_\odot$  and total mass of  $1000M_\odot$ . Figure 6.2 shows the evolution of the mass of the cluster with time for 9 of the models. The mass loss is initially the same for all models since in this stage it is dominated by stellar evolution of the heaviest stars. After about 100 Myr clusters in the heaviest halos keep losing mass at a faster pace than the clusters in the lighter halos. In these heavier halos the effect of concentration is also clearly visible. A higher concentration means a faster disruption. More of the mass is concentrated in the centre resulting in a greater tidal force on the cluster. For the least massive halos the effects of concentration become negligible. Remarkable also is the fact that for low concentrations the mass loss is the same for low and intermediate mass halos.

These simulations were repeated with the cluster at an orbital distance of 4.5 kpc. Their mass loss is shown in Figure 6.3. The same relative trends are visible. For more massive halos putting the cluster on a smaller orbital distance results in a faster mass loss.

To quantify the disruption of a cluster I have defined the disruption time scale as the time it takes for the cluster to lose half of its mass. This is shown in Figure 6.4. Generally more massive halos disrupt faster than lighter halos. In massive halos the concentration has large effect on the disruption time while in the lower mass ranges the disruption is independent of mass and concentration. Variations in this regime are dominated by statistical effects (each simulation is only done once, see Appendix A for a discussion). Figure 6.5 shows the results for the models at an orbital distance of 4.5 kpc. For high mass halos the disruption time scale drops when the cluster is put on this smaller orbital distance. For intermediate mass halos it drops at high concentrations while for the lowest mass halo there is no significant difference.

The model with virial halo mass of  $1.5 \times 10^{12}M_\odot$  and concentration  $c = 10$  resembles closest a model for our galactic halo and from now on I will call it the standard model. Figures 6.6 and 6.7 show the mass evolution and the disruption time scale for this standard model at four different orbital distances. A closer orbit means a faster disruption.

The half mass relaxation time scales for different models are shown in figures 6.8, ?? and 6.9. More massive halos result in a shorter relaxation time for the cluster. For the more massive halos also a higher concentration means faster relaxation. Owing to a faster loss of stars the half mass radius decreases faster in clusters in massive halos resulting in a shorter relaxation time (c.f. Equation 3.11). A shorter orbital distance results in a faster

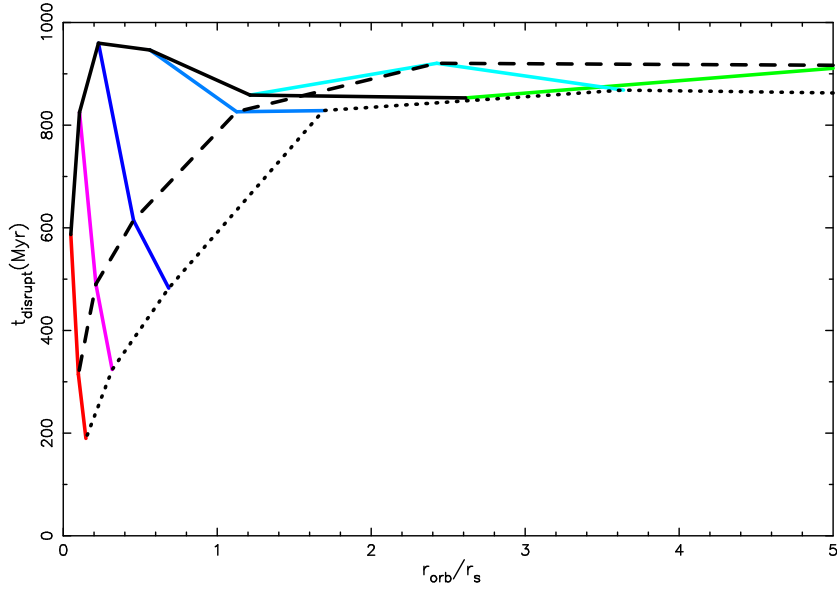


Figure 6.4: The disruption time as a function of orbital distance of scale length for all models at orbital distance of 8.5 kpc. Coloured lines connect models with equal virial mass -  $10^9 M_\odot$  (green),  $10^{10} M_\odot$  (cyan),  $10^{11} M_\odot$  (light blue),  $1.5 \times 10^{12} M_\odot$  (blue),  $10^{13} M_\odot$  (magenta) and  $10^{14} M_\odot$  (red) - and black lines connect models with equal concentration - 5 (solid), 10 (dashed) and 15 (dotted).

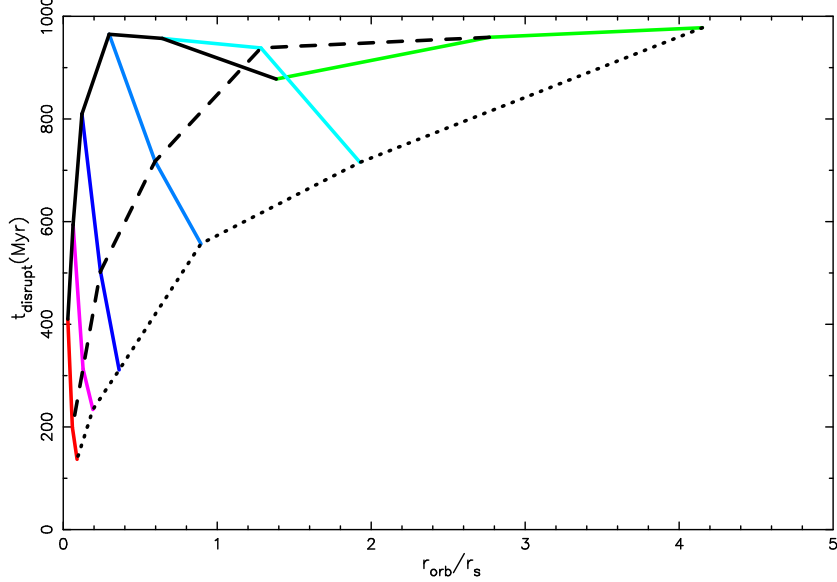


Figure 6.5: The disruption time as a function of orbital distance of scale length for all models at orbital distance of 4.5 kpc. Labels as in figure 6.4.

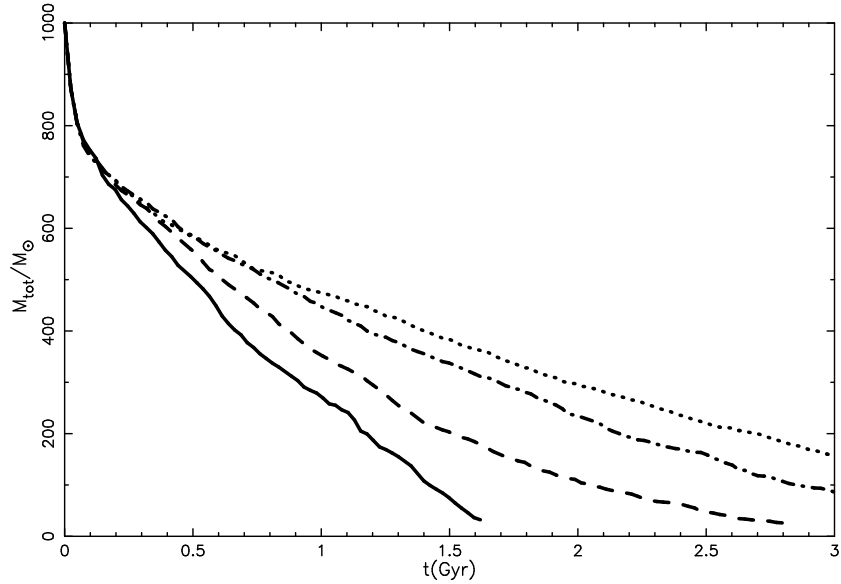


Figure 6.6: The mass loss for the standard model ( $M_{vir} = 1.5 \times 10^{12} M_{\odot}$ ,  $c = 10$ ) at different orbital distances - 4.5 kpc (solid), 8.5 kpc (dashed), 17.0 kpc (dashed-dotted) and 34.0 kpc (dotted).

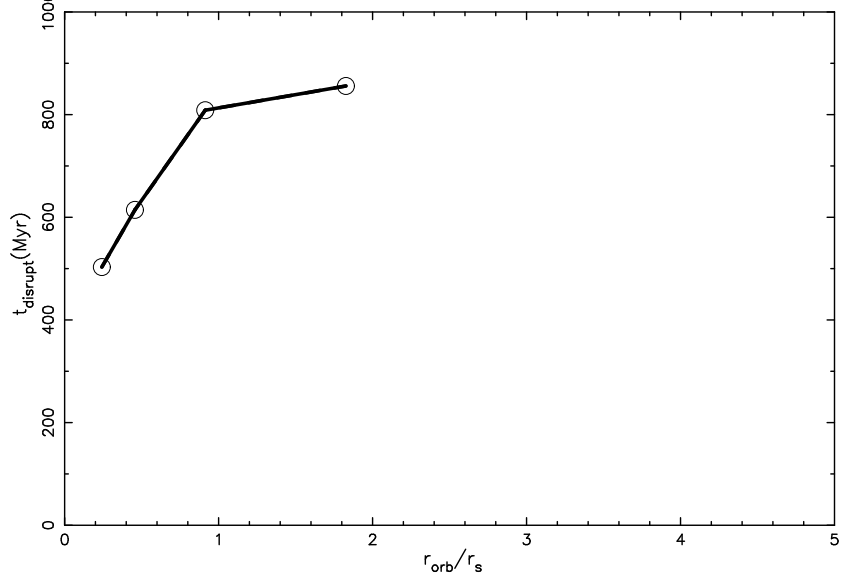


Figure 6.7: The disruption time for the standard model ( $M_{vir} = 1.5 \times 10^{12} M_{\odot}$ ,  $c = 10$ ) at different orbital distances - 4.5 kpc, 8.5 kpc, 17.0 kpc and 34.0 kpc.

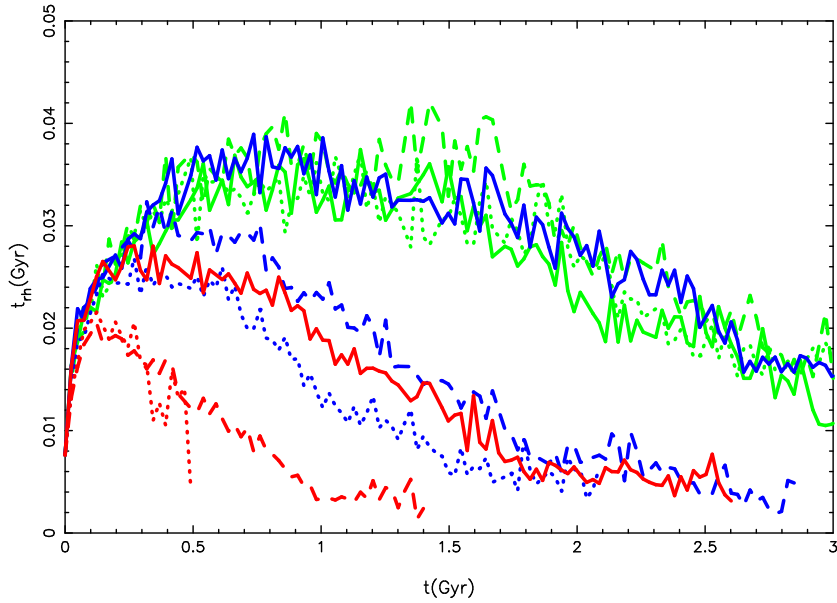


Figure 6.8: The half mass relaxation time scale for models on a orbital distance of 8.5 kpc. Labels as in figure 6.4.

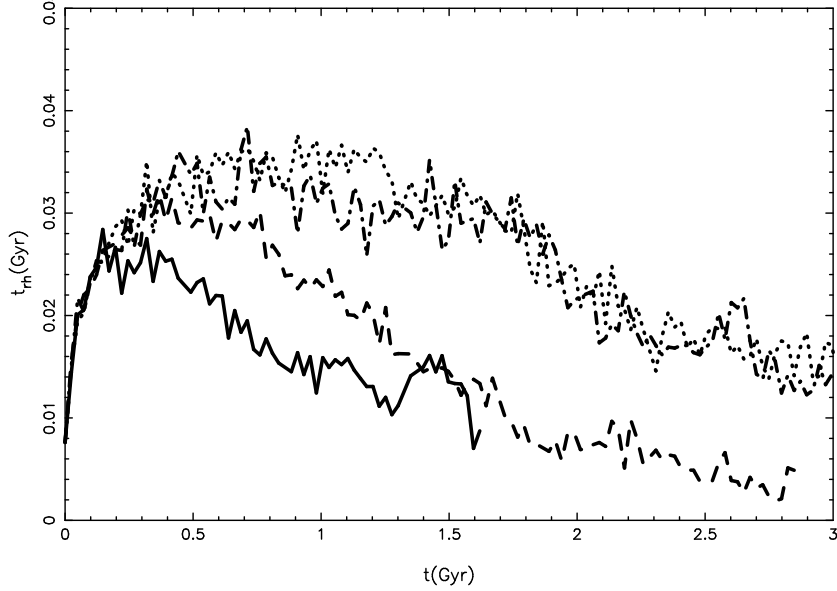


Figure 6.9: The half mass relaxation time scale for the standard model at different orbital distances. Labels as in figure 6.7.

evolution of the relaxation time. The peak half mass relaxation time is also a bit smaller at shorter orbital distances.

I also looked at the influence of the halo on the evolution of the core radius over half-mass radius. As we have already seen in Chapter 5 an external tidal field does not have a large influence on core collapse and that is what I found again when including a dark matter halo. However including a very heavy halo results in fast disruption even before the core has time to collapse.

### 6.5.3 Putting the galaxy in the halo

Here I have included the modelIII galaxy described in Section 6.5.1 to a subset of the models at orbital distance 8.5 kpc described above (Model IV). Figures 6.10, 6.11 and 6.12 show the mass, disruption time and relaxation time respectively for these models. Adding the galaxy results in a faster mass loss and thus shorter disruption time and relaxation time for the cluster. This is to be expected because this is just an addition of mass. The relative effect is greatest on the lowest mass halos because the size of the galaxy is relatively larger compared to their halo size than for larger halos.

Finally I ran a simulation for the standard model with all the galactic mass in the bulge (Model V). This results in an ever faster disruption. The mass loss for Model III, Model IV and Model V are shown in figure 6.13. All my models are on orbits in the disc. However I did run a model with an orbit perpendicular to the disc which resulted in earlier disruption owing to "disk shocking": the cluster experiences a sudden change in the potential as it goes through the disk resulting in faster mass loss.

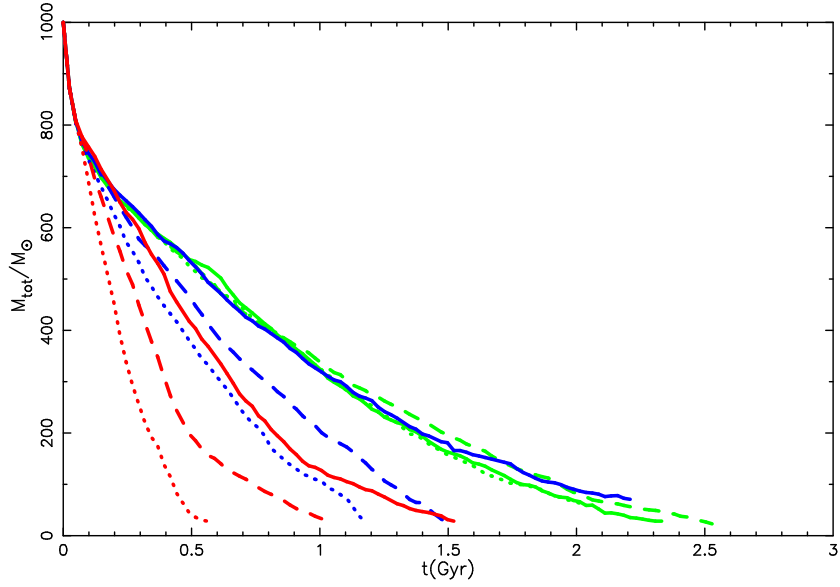


Figure 6.10: The total mass evolution for a cluster at an orbital distance of 8.5 kpc including a full galactic model. Labels as in figure 6.2

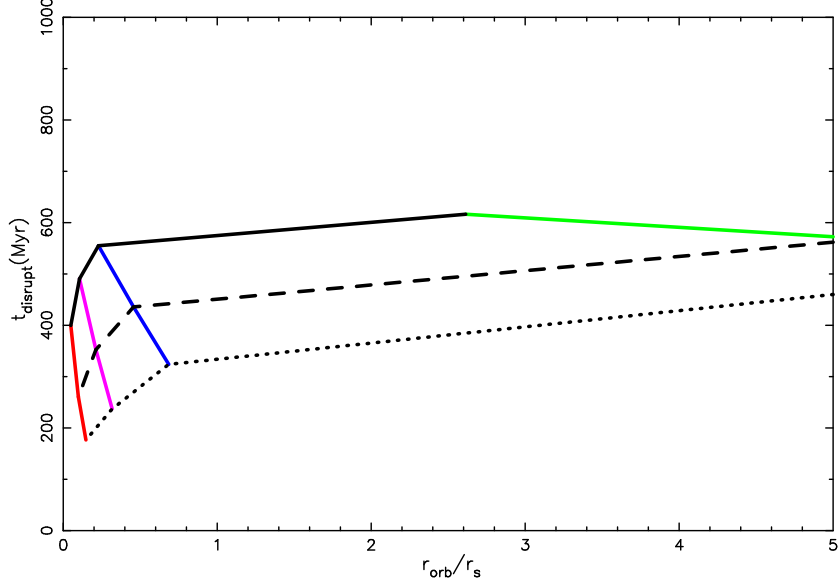


Figure 6.11: The disruption times for clusters at an orbital distance of 8.5 kpc including a full galactic model. Labels as in figure 6.4

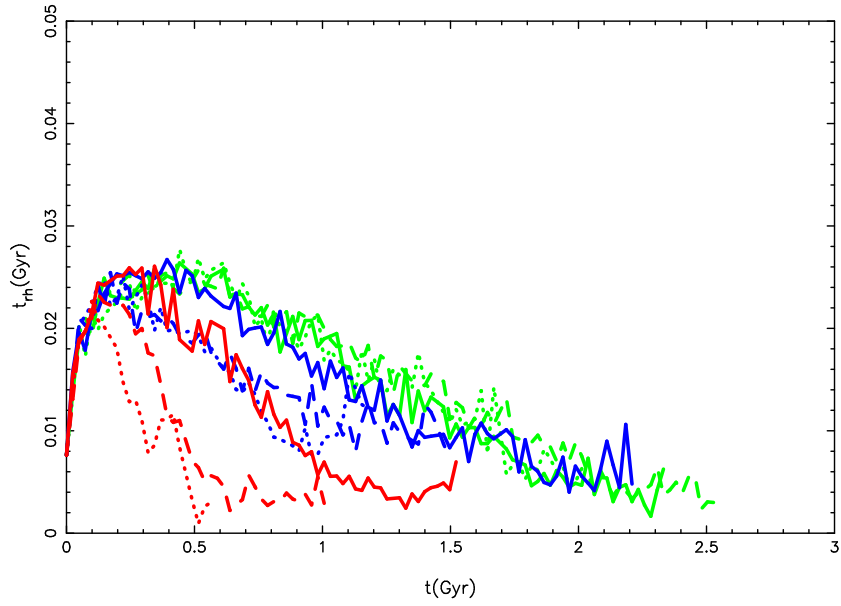


Figure 6.12: Half mass relaxation time for a cluster at an orbital distance of 8.5 kpc including a full galactic model. Labels as in figure 6.2

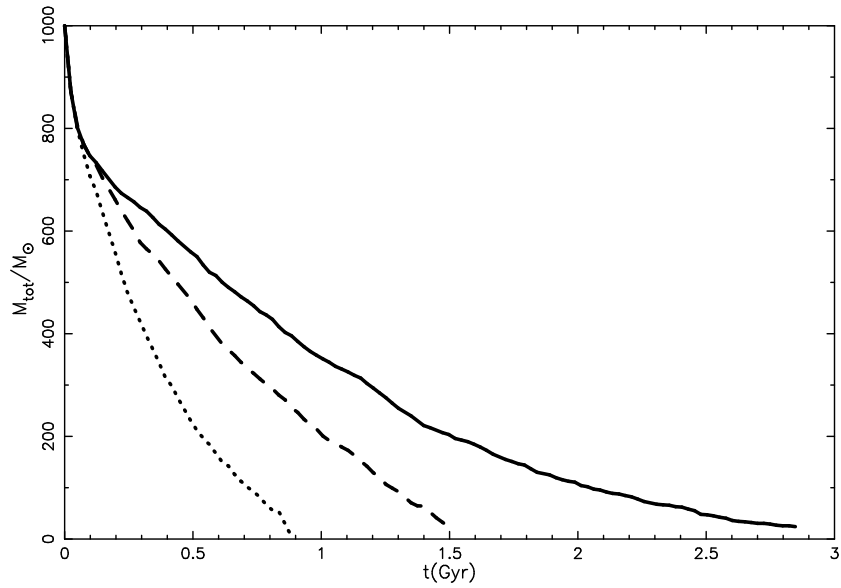


Figure 6.13: The total mass evolution for the standard model. The solid line is the cluster in a pure NFW halo (Model III), the dashed line in a NFW halo with a full galactic model added (Model IV) and the dotted line a NFW halo with all the galactic mass in the bulge (Model V).

# Chapter 7

## The generalized NFW profile

### 7.1 Generalized NFW profile

The generalised NFW profile is, as the name would suggest, a more general form of the NFW dark matter halo mass profile in which the inner logarithmic slope  $\alpha$  is free to vary between  $0 \leq \alpha < 3$ , rather than  $\alpha=1$  as is the case for the NFW profile, while the outer logarithmic slope asymptotes to  $-3$  at large radii. Formally this is written as

$$\rho(r) = \frac{\rho_{\text{crit}}\delta_c}{(r/r_s)^\alpha(1+r/r_s)^{3-\alpha}}, \quad (7.1)$$

where again  $r_s$  is the scale radius,  $\rho_{\text{crit}}$  the critical density of the Universe at  $z = 0$  and  $\delta_c$  the characteristic overdensity.

Equation 7.1 is then integrated over the volume enclosed within the virial radius, which gives

$$M_{\text{vir}} = 4\pi\delta_c\rho_{\text{crit}}r_s^3 \int_0^c \frac{u^{2-\alpha}}{(1+u)^{3-\alpha}} du. \quad (7.2)$$

where  $c = r_{\text{vir}}/r_s$  is the concentration parameter. This is equivalent to Equation 6.3. The integral in equation 7.2 is a representation of the hypergeometric function (cf. equation 3.194.1 of Gradshteyn & Ryzhik, 1994)

$$\int_0^u \frac{x^{\mu-1}}{(1+\beta x^\nu)} dx = \frac{u^\nu}{\nu} {}_2F_1(\nu, \mu; 1+\mu; -\beta u) \quad (7.3)$$

where  $\mu = 3 - \alpha$ ,  $\nu = 3 - \alpha$ ,  $\beta = 1$  and  $u = r_{\text{vir}}/r_s = c_{\text{vir}}$ . Substituting this into equation 7.2 gives

$$M_{\text{vir}} = \frac{4\pi}{3-\alpha} \delta_c \rho_{\text{crit}} r_s^3 c_{\text{vir}}^{3-\alpha} {}_2F_1(3-\alpha, 3-\alpha; 4-\alpha; -c_{\text{vir}}) \quad (7.4)$$

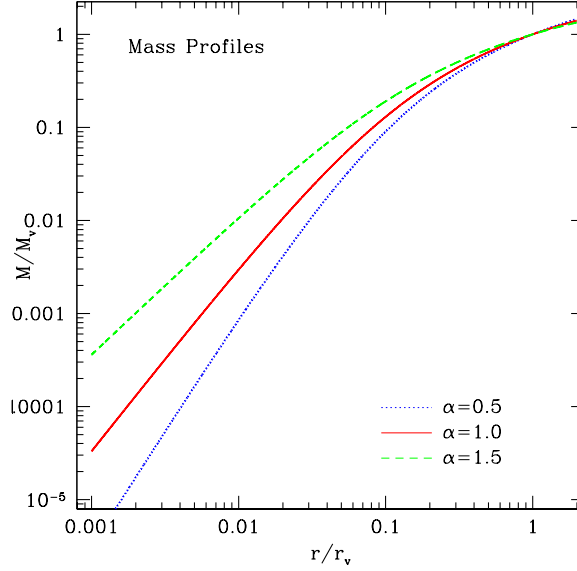


Figure 7.1: This figure shows how the enclosed mass varies with radius in the  $\alpha = 0.5$  (dotted),  $\alpha = 1.0$  (solid) and  $\alpha = 1.5$  (dashed) halo models.  $M_v$  is the virial halo mass and  $r_v$  is the virial radius of the halo.

This can be compared with equation 6.3 to give

$$\delta_c = \Delta_{\text{vir}} \frac{(3 - \alpha)}{3} c_{\text{vir}}^\alpha \frac{1}{{}_2F_1(3 - \alpha, 3 - \alpha; 4 - \alpha; -c_{\text{vir}})}. \quad (7.5)$$

Once  $\delta_c$  is known, it is straightforward to compute the mass enclosed within a radius  $r$ ,

$$M(r) = \frac{4\pi}{3 - \alpha} \delta_c \rho_{\text{crit}} r_s^3 (r/r_s)^{3-\alpha} {}_2F_1(3 - \alpha, 3 - \alpha; 4 - \alpha; -r/r_s) \quad (7.6)$$

Figure 7.1 illustrates the dependence of the enclosed mass on the value of  $\alpha$  for a  $10^{12} M_\odot$  halo with concentration  $c = 10$ . As one expects, increasing  $\alpha$  results in more mass enclosed with a given radius.

## The Gravitational Potential and Acceleration

The gravitational potential can be determined by calculating

$$\Phi(r) = -4\pi G \left( \frac{1}{r} \int_0^r \rho(r) r^2 dr + \int_r^\infty \rho(r) r dr \right) \quad (7.7)$$

The first of these integrals ( $\int_0^r \rho(r)r^2 dr$ ) should be familiar from equation 7.2; the second ( $\int_r^\infty \rho(r)r dr$ ) requires again use of the hypergeometric function (cf. equation 3.194.1 of Gradshteyn & Ryzhik, 1994)

$$\int_u^\infty \frac{x^{\mu-1}}{(1+\beta x)^\nu} dx = \frac{u^{\mu-\nu}}{\beta^\mu(\nu-\mu)} {}_2F_1(\nu, \nu-\mu; \nu-\mu+1; -1/\beta u) \quad (7.8)$$

which gives

$$\int_r^\infty \rho(r)r dr = \frac{1}{r/r_s} {}_2F_1(3-\alpha, 1; 2; -\frac{1}{r/r_s}). \quad (7.9)$$

Therefore the gravitational potential  $\Phi(r)$  at radius  $r$  is given by

$$\Phi(r) = -\frac{4\pi G \delta_c \rho_{\text{crit}} r_s^2}{r/r_s} \left[ \frac{1}{3-\alpha} \left(\frac{r}{r_s}\right)^{3-\alpha} {}_2F_1 + {}_2F_1' \right]. \quad (7.10)$$

where  ${}_2F_1'$  represents  ${}_2F_1(3-\alpha, 1; 2; -1/r/r_s)$  and  ${}_2F_1$  represents  ${}_2F_1(3-\alpha, 3-\alpha; 4-\alpha; -r/r_s)$ .

Figure 7.1 illustrates the dependence of the escape velocity, which is a useful measure of the local potential ( $v_{\text{esc}} = \sqrt{2|\Phi|}$ ) on  $\alpha$  for a  $10^{12} M_\odot$  halo with concentration  $c = 10$ . The velocity a test particle requires to escape from a given radius increases as the inner slope increases at small radii.

The gravitational acceleration is more straightforward to compute;

$$\begin{aligned} \vec{a}(\vec{r}) &= -\frac{\partial \Phi}{\partial r} \hat{e}_r \\ &= -\frac{GM(r)}{r^2} \hat{e}_r \end{aligned} \quad (7.11)$$

where  $\hat{e}_r = \vec{r}/r$  is the unit vector in the radial direction. The gradient in the acceleration (which is required for calculating the time derivative of the acceleration) is

$$\vec{\nabla} \cdot \vec{a} = \frac{\partial a}{\partial r} = -\frac{G}{r^2} \left( \frac{dM}{dr} - \frac{2M(r)}{r} \right), \quad (7.12)$$

which gives

$$4\pi G \rho_{\text{crit}} \delta_c \left( \frac{(r/r_s)^{-\alpha}}{(1+r/r_s)^{3-\alpha}} - 2 \left(\frac{r}{r_s}\right)^{-\alpha} \frac{{}_2F_1}{(3-\alpha)} \right) \quad (7.13)$$

where again  ${}_2F_1$  represents  ${}_2F_1(3-\alpha, 3-\alpha; 4-\alpha; -r/r_s)$  for compactness.

Figure 7.3 shows how the acceleration depends on  $\alpha$  for our fiducial  $10^{12} M_\odot$  halo with a concentration  $c = 10$ .

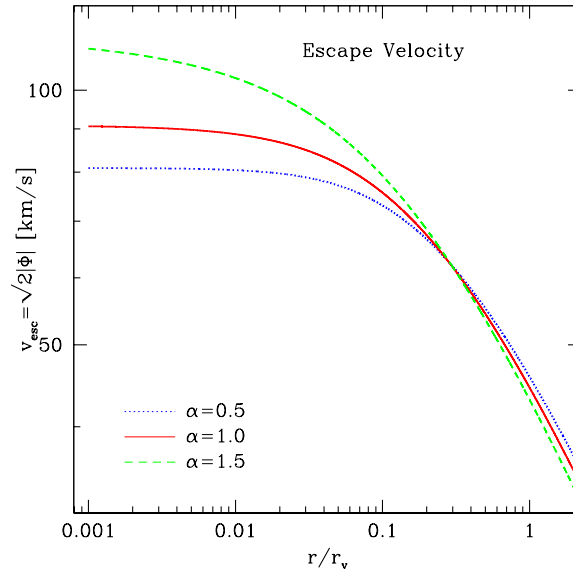


Figure 7.2: The escape velocity  $v_{\text{esc}}$  represents the minimum speed a test particle requires to climb out of the halo potential and escape to infinity. It provides a convenient measure of the gravitational potential at a particular radius –  $v_{\text{esc}} = \sqrt{2|\Phi|}$ . This figure shows how the escape velocity varies with radius in the  $\alpha = 0.5$  (dotted),  $\alpha = 1.0$  (solid) and  $\alpha = 1.5$  (dashed) halo models.

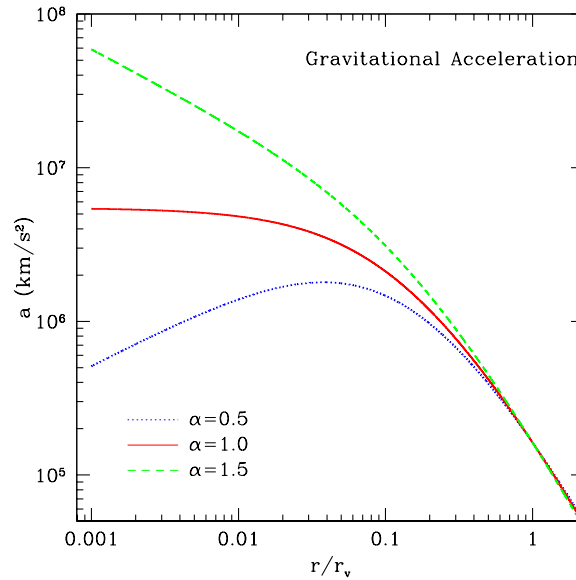


Figure 7.3: This figure shows how the gravitational acceleration varies with radius in the  $\alpha = 0.5$  (dotted),  $\alpha = 1.0$  (solid) and  $\alpha = 1.5$  (dashed) halo models.

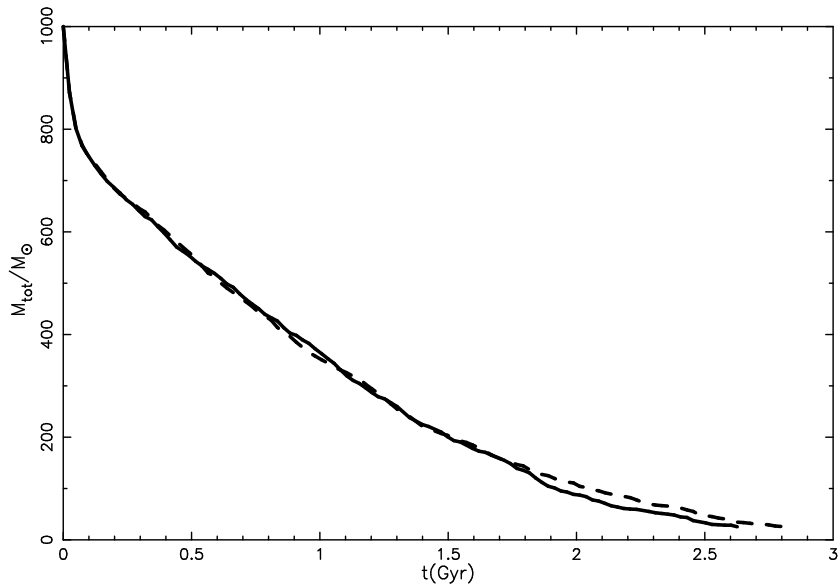


Figure 7.4: This figure shows the mass evolution for the standard model defined in the previous chapter using the `gnfw` subroutine (solid) and the `fnfw` subroutine (dashed).

## 7.2 Addition to `nbody6`

To add the possibility of a halo with a generalised NFW profile I have written a subroutine `gnfw` that reads in the force and force derivatives from an existing table. The values in these tables are computed beforehand using a routine that includes a numerical evaluation of the hypergeometric function 7.3. This is now incorporated into the code in the same way as `fnfw` described in Section 6.4. `nbody6` is manipulated to use this subroutine by giving the virial mass a negative value. All the other input required for the halo is then read in from the table. Figure 7.4 shows the mass loss for the standard model ( $M_{vir} = 1.5 \times M_{\odot}$ ,  $c = 10$ ) with  $\alpha = 1.0$  (standard NFW profile) using the new subroutine `gnfw` together with the mass loss for the same model using `fnfw`. The two have the same mass loss history so I can be confident that the new routine works properly.

## 7.3 Results

Here I show the results using the generalized NFW profile. All models have the same halo mass ( $1.5 \times 10^{12} M_{\odot}$ ). Again I used three different concentra-

tions  $c$  (5, 10 and 15) and seven different values of  $\alpha$  ranging from 0 to 1.5 in steps of 0.25 resulting in 21 models in total. In all models the cluster is at a circular orbit at a distance of 8.5 kpc from the galactic centre. Figures 7.5, 7.6 and 7.7 each show the evolution of the total mass for the seven different values of  $\alpha$  at a given concentration. For the highest concentration halo ( $c=15$ ) there is a clear trend of increasing mass loss with increasing  $\alpha$ . However moving to lower concentrations this effect starts to turn around at the least cuspy halos. This is also clearly seen in the disruption plot. There is maximum in the disruption time for the  $c=5$  case at  $\alpha = 0.50$ . So in a halo with a low concentration parameter, an extreme decrease of  $\alpha$  leads to faster disruption.

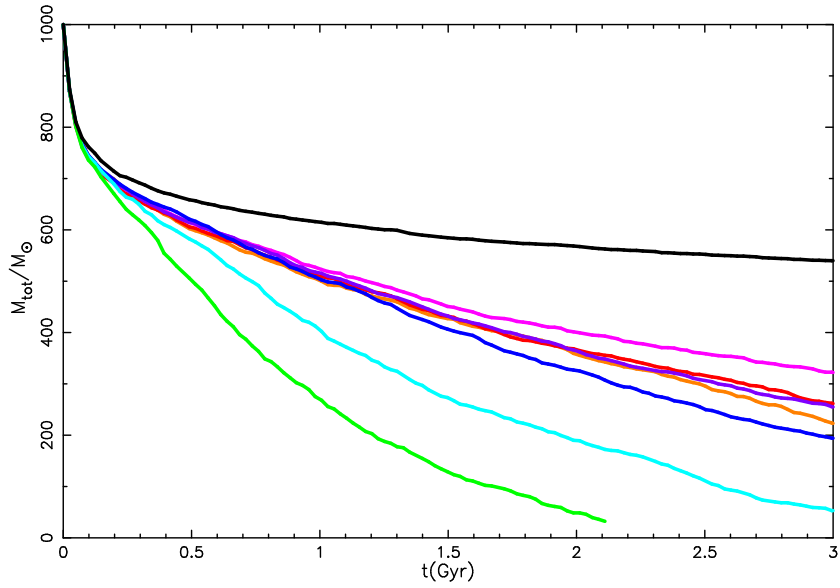


Figure 7.5: This plot shows the evolution of the total mass for different values of  $\alpha$  - 0.0 (orange), 0.25 (red), 0.50 (magenta), 0.75 (purple), 1.0 (blue), 1.25 (cyan) and 1.5 (green) - for a halo with virial mass  $1.5 \times 10^{12} M_{\odot}$  and concentration parameter  $c = 5$ . To see the effect of the external tidal field the mass evolution for an isolated cluster is shown (black) where stellar evolution is the only mechanism by which the cluster can lose mass.

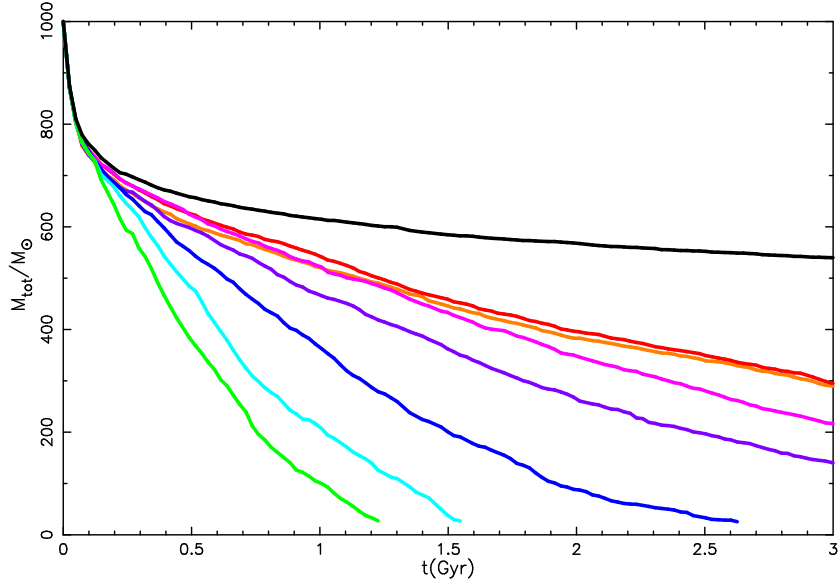


Figure 7.6: This plot shows the evolution of the total mass for different values of  $\alpha$  for a halo with virial mass  $1.5 \times 10^{12} M_{\odot}$  and concentration parameter  $c = 10$ . Labels as in Figure 7.5

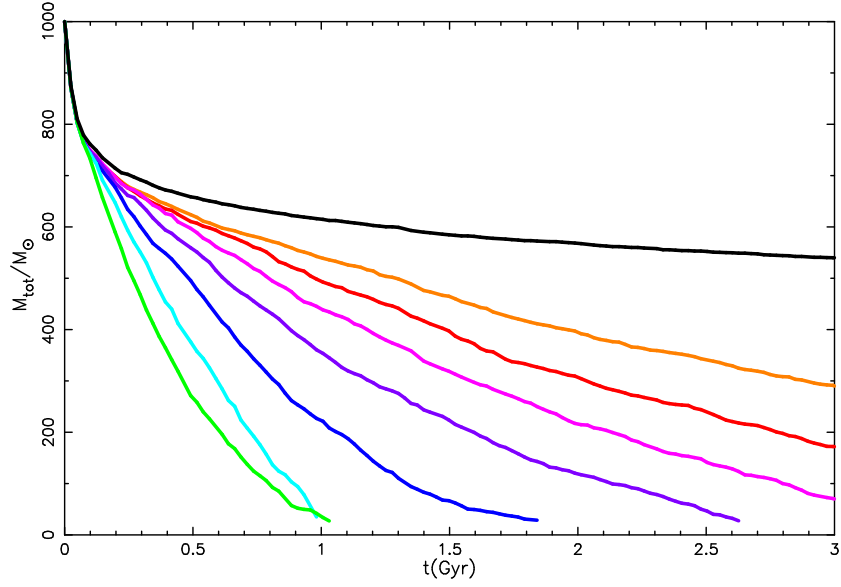


Figure 7.7: This plot shows the evolution of the total mass for different values of  $\alpha$  for halo with virial mass  $1.5 \times 10^{12} M_{\odot}$  and concentration parameter  $c = 15$ . Labels as in Figure 7.5

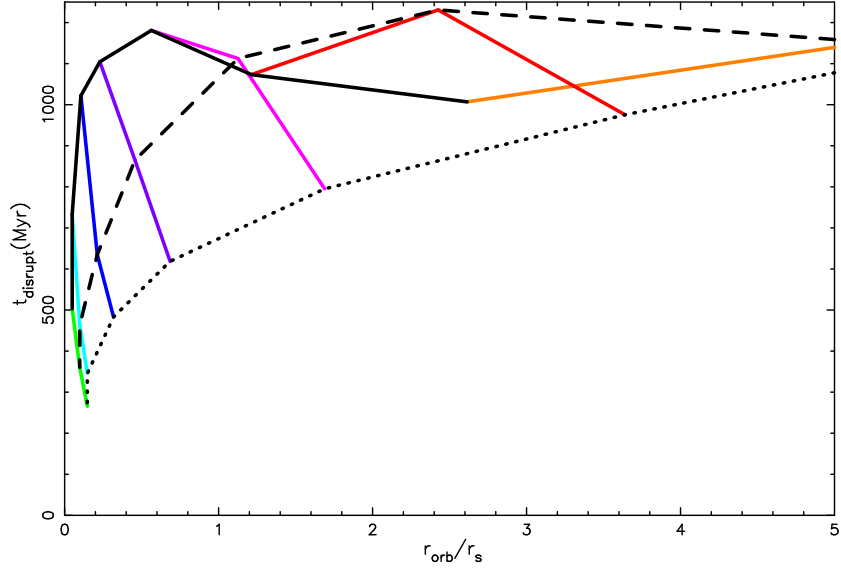


Figure 7.8: The disruption time for different values of  $\alpha$  (colours as in Figure 7.5 and  $c = 5$  (solid), 10 (dashed) and 15 (dotted) - for a halo with virial mass  $1.5 \times 10^{12} M_{\odot}$ .

# Chapter 8

## Conclusions

From this study I can conclude that an underlying dark matter halo is important for globular cluster evolution. Moreover the structure of the halo has a significant effect on the disruption rate. This is interesting from a theoretical perspective, and is an important confirmation for those who are interested in globular cluster evolution. However, it may also be significant in a broader context. The favoured cosmological model predicts that galaxies should live in cuspy dark matter halos. Previous studies of globular cluster evolution have been of clusters that evolve in non-cuspy potentials. Inferences have been drawn from these simulations of general processes such as core-collapse and mass-segregation and observations of globular clusters, which the simulations seem to do a good job of reproducing. We do not appear to need cuspy dark matter halos to produce these trends in simulated globular clusters that are consistent with observational data, so does this imply that cuspy dark matter halos are not needed at all? This is not straightforward to answer, because it is not understood how the assembly of the galaxy has affected its dark matter halo, and whether this has effectively wiped out the cusp (as would appear necessary from rotation curve studies of dark matter dominated galaxies). However, if cusps are robust in the presence of the growing galaxy, then it may have implications for our understanding of globular cluster evolution.

More speculatively, the enhanced rate of disruption of clusters in cuspy halos has interesting implications for their use as probes of galaxy formation. Understanding how efficiently globular clusters form should provide us with insight into the efficiency of galaxy formation at high redshifts. The number of old globular clusters today could tell us how plentiful the sites of globular cluster formation were in the past, which in turn tells us about the efficiency with which gas cooled and formed molecular clouds. These sites may be regulated by the location (in the discs of gas-rich proto-galaxies, in mergers

between gas-rich proto-galaxies) or the ambient radiation field (cosmological reionisation). If globular clusters are disrupted more efficiently in cuspy halos, then we could be missing a large fraction of globular clusters thus misinterpreting observations and drawing even more uncertain conclusions.

As to the questions posed in the introduction I can say that the presence of a dark matter halo and its internal structure have an effect on all of the issues addressed. However at this stage it is too early to make any quantitative statements. But the results presented in this thesis show that the disruption of globular cluster in the presence of a dark matter halo has an important contribution and should be investigated further.

## 8.1 Future work

The halos that I have treated here are highly simplified with respect to what is known about their structure. The NFW profile is spherical and smooth. Also the halos used in my simulations do not evolve over time. However cosmological simulations show that dark matter halos are aspherical and asymmetric and evolve over time. As far as analytic halos are concerned their evolution over time can be modeled as a sequence of models treated in this thesis (accreting material thus becoming heavier and less concentrated). The next step is to actually link cosmological simulations to star cluster simulations. Values for a simulated halo can be tabulated and read into `nbody6` in the same manner as described for the generalised profile taking this study to the next level of more realistic halos.

Also it should be interesting to expand the cluster size to a full sized globular cluster. I ran an  $N = 16000$  star cluster simulation for the standard model. The disruption is of course slower due to the larger number of stars but scaling by the relaxation time gives similar results. This gives confidence that my results will hold for larger systems as well.

In this study I have looked at clusters on circular orbits. Real globular clusters are generally on eccentric orbits. Varying the orbital distance and eccentricity of the orbit and also orientation with respect to the galactic disk (if present) is certainly interesting.

# Appendix A

## Comparison of identical models with different random number seeds

All data presented in this thesis are the result of one realisation of every model. Each input file takes a random number seed which is used to generate the initial distribution of the stars in the system. The following figures show that variations between different realisations of the same model are small and do not have an effect on the general conclusions drawn. However for the lightest halo in Model III ( $M_{vir} = 10^9 M_{\odot}$ ) the disruption times of the two simulations are of order 100 Myrs apart as can be seen in Figure A.1. For all other models the differences are only a few Myrs with the exception of the heaviest halo where the difference is of order 40 Myrs. Hence results discussed in Chapter 6 and 7 are indeed influenced by statistical noise but overall observed trends hold.

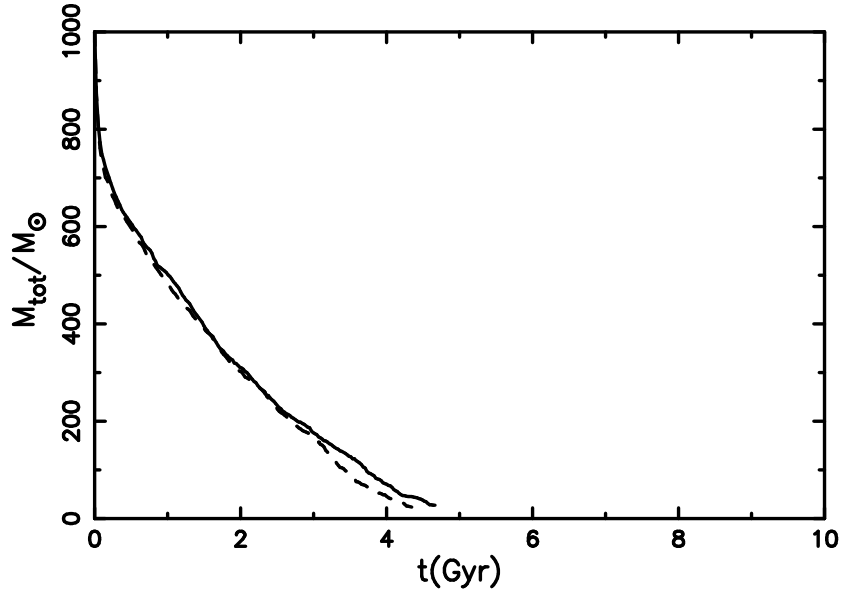


Figure A.1: The evolution of the total mass of two different realisations of the Model III with  $M_{vir} = 10^9 M_{\odot}$  and  $c = 10$ .

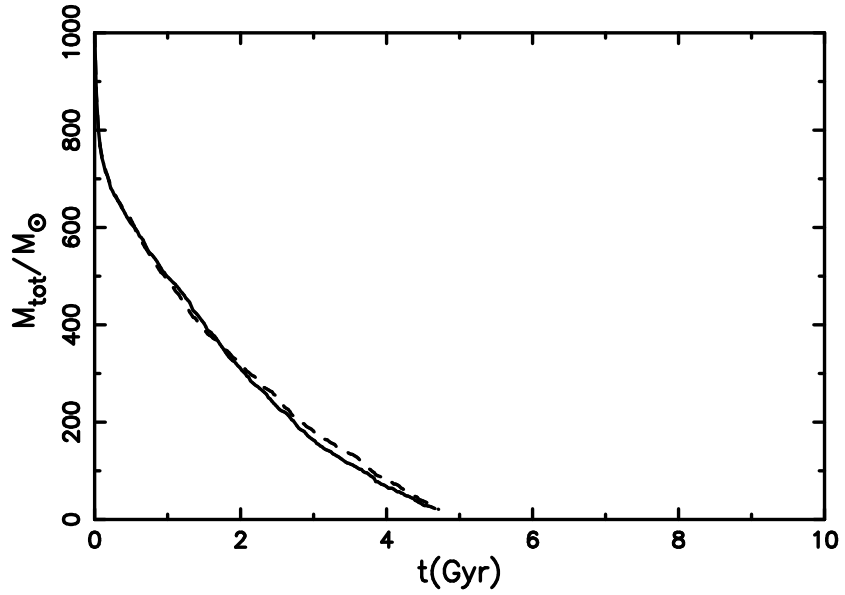


Figure A.2: The evolution of the total mass of two different realisations of the Model III with  $M_{vir} = 1.5 \times 10^{12} M_{\odot}$  and  $c = 5$ .

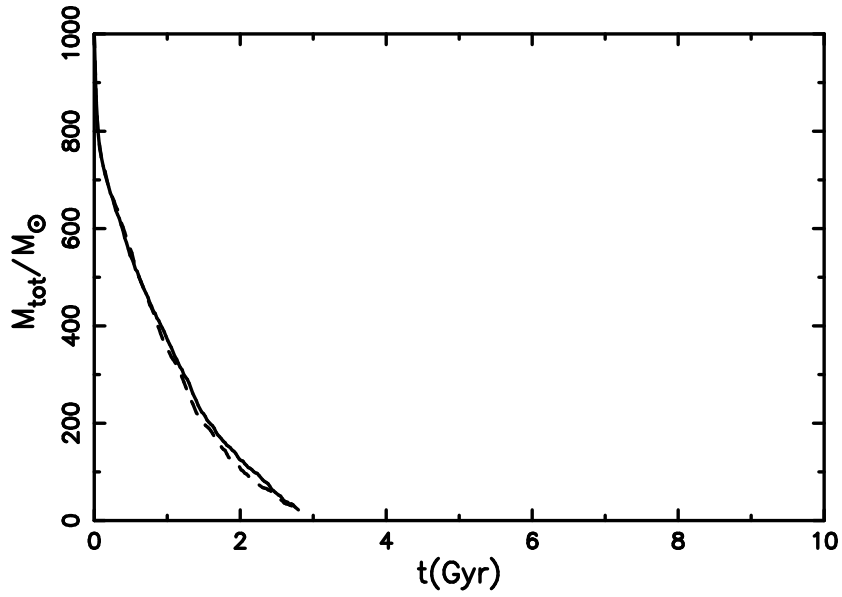


Figure A.3: The evolution of the total mass of two different realisations of the Model III with  $M_{vir} = 1.5 \times 10^{12} M_{\odot}$  and  $c = 10$ .

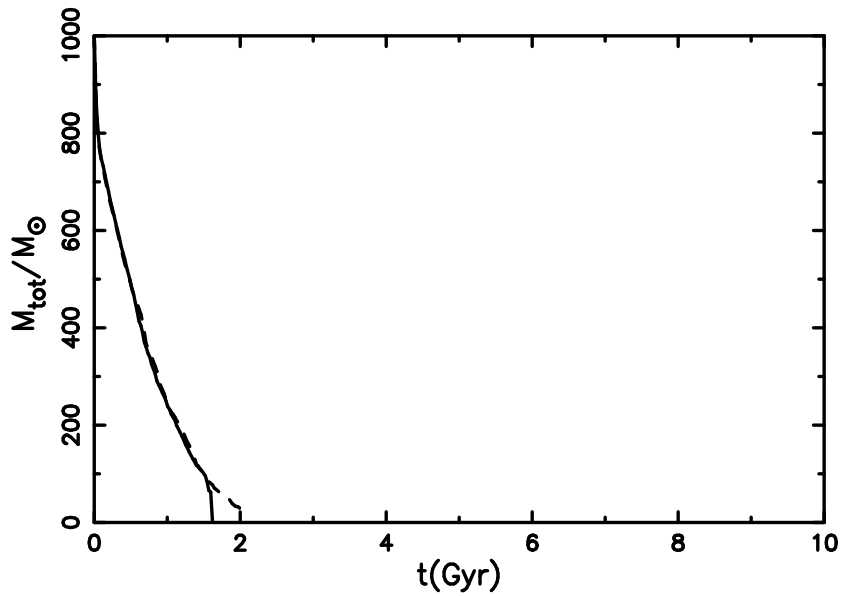


Figure A.4: The evolution of the total mass of two different realisations of the Model III with  $M_{vir} = 1.5 \times 10^{12} M_{\odot}$  and  $c = 15$ .

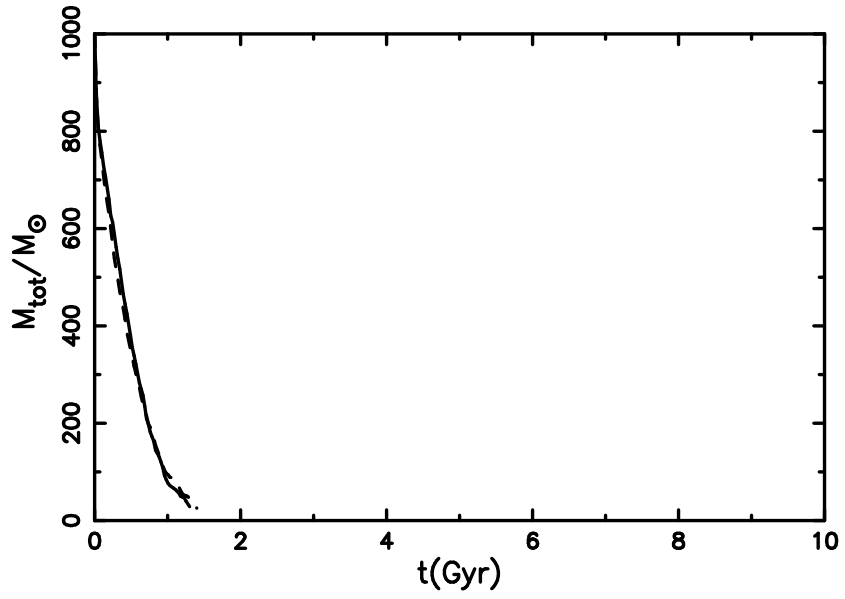


Figure A.5: The evolution of the total mass of two different realisations of the Model III with  $M_{\text{vir}} = 10^{14} M_{\odot}$  and  $c = 10$ .

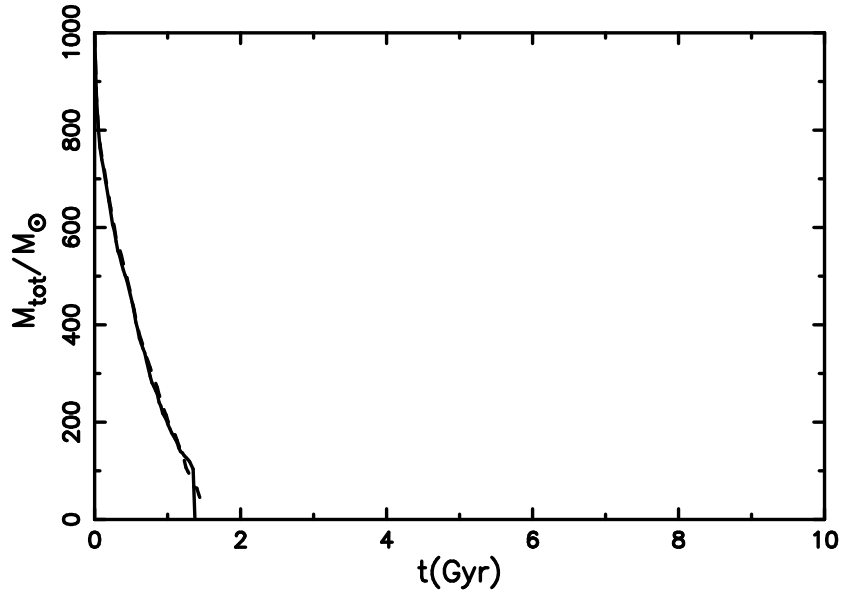


Figure A.6: The evolution of the total mass of two different realisations of the Model IV with  $M_{\text{vir}} = 1.5 \times 10^{12} M_{\odot}$  and  $c = 10$ .

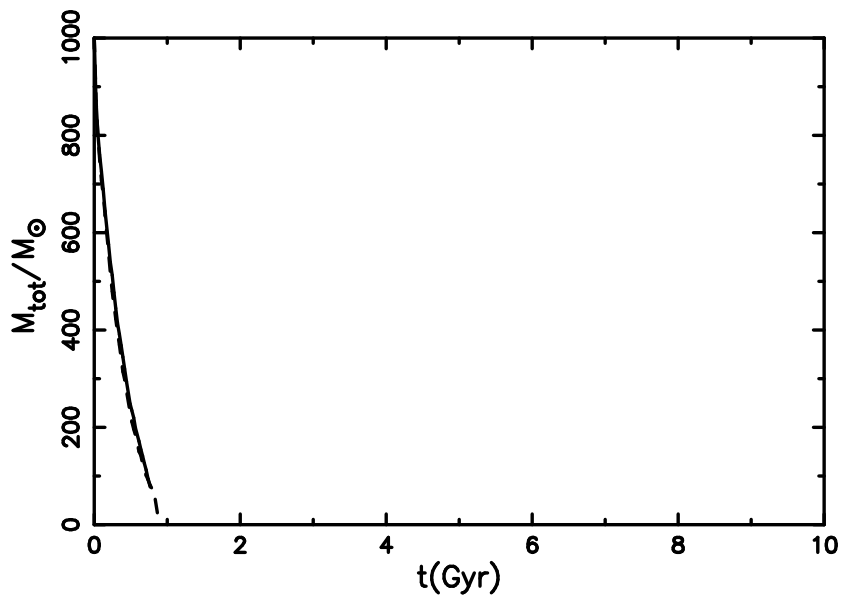


Figure A.7: The evolution of the total mass of two different realisations of the Model V with  $M_{\text{vir}} = 1.5 \times 10^{12} M_{\odot}$  and  $c = 10$ .

# Bibliography

- Aarseth, S. J. 1985, in *Multiple time scales*, p. 377 - 418, 377–418
- Aarseth, S. J. 1994, in *Lecture Notes in Physics*, Berlin Springer Verlag, Vol. 433, *Galactic Dynamics and N-Body Simulations*, ed. G. Contopoulos, N. K. Spyrou, & L. Vlahos, 277–312
- Aarseth, S. J. 2001, *New Astronomy*, 6, 277
- Aarseth, S. J. 2003, *Gravitational N-Body Simulations (Gravitational N-Body Simulations, by Sverre J. Aarseth, pp. 430. ISBN 0521432723. Cambridge, UK: Cambridge University Press, November 2003.)*
- Aarseth, S. J. & Fall, S. M. 1980, *ApJ*, 236, 43
- Aarseth, S. J. & Zare, K. 1974, *Celestial Mechanics*, 10, 185
- Ahmad, A. & Cohen, L. 1973, *Journal of Computational Physics*, 12, 389
- Bailin, J. & Steinmetz, M. 2005, *ApJ*, 627, 647
- Baugh, C. M. 2006, *Reports of Progress in Physics*, 69, 3101
- Binney, J. & Tremaine, S. 1987, *Galactic dynamics (Princeton, NJ, Princeton University Press, 1987, 747 p.)*
- Bower, R. G., Benson, A. J., Malbon, R., et al. 2006, *MNRAS*, 370, 645
- Brodie, J. P. & Strader, J. 2006, *ARA&A*, 44, 193
- Burden, R. L. & Faires, J. D. 2001, *Numerical analysis (Numerical analysis by Richard L. Burden and J. Douglas Faires, 7th ed., Pacific Grove, CA: Brooks/Cole, 2001. ISBN 0534382169)*
- Casertano, S. & Hut, P. 1985, *ApJ*, 298, 80
- Chaboyer, B. & Krauss, L. M. 2002, *ApJ*, 567, L45

- Cole, S. & Lacey, C. 1996, MNRAS, 281, 716
- Croton, D. J., Springel, V., White, S. D. M., et al. 2006, MNRAS, 365, 11
- Eke, V. R., Cole, S., Frenk, C. S., & Navarro, J. F. 1996, MNRAS, 281, 703
- Gao, L. & White, S. D. M. 2006, MNRAS, 373, 65
- Gao, L., White, S. D. M., Jenkins, A., Stoehr, F., & Springel, V. 2004, MNRAS, 355, 819
- Giersz, M. & Heggie, D. C. 1997, MNRAS, 286, 709
- Hansen, B. M. S., Brewer, J., Fahlman, G. G., et al. 2002, ApJ, 574, L155
- Heggie, D. C. & Mathieu, R. D. 1986, in Lecture Notes in Physics, Berlin Springer Verlag, Vol. 267, The Use of Supercomputers in Stellar Dynamics, ed. P. Hut & S. L. W. McMillan, 233–+
- Hurley, J. R., Aarseth, S. J., & Shara, M. M. 2007, ApJ, 665, 707
- Hurley, J. R., Pols, O. R., & Tout, C. A. 2000, MNRAS, 315, 543
- Hurley, J. R. & Shara, M. M. 2003, ApJ, 589, 179
- King, I. 1962, AJ, 67, 471
- King, I. R. 1966, AJ, 71, 64
- Kravtsov, A. V. & Gnedin, O. Y. 2005, ApJ, 623, 650
- Kustaanheimo, P. & Stiefel, E. 1965, J. Reine Angew. Math., 218, 204
- Mashchenko, S. & Sills, A. 2005, ApJ, 619, 258
- Miyamoto, M. & Nagai, R. 1975, PASJ, 27, 533
- Navarro, J. F., Frenk, C. S., & White, S. D. M. 1996, ApJ, 462, 563
- Ostriker, J. P. 1985, in IAU Symposium, Vol. 113, Dynamics of Star Clusters, ed. J. Goodman & P. Hut, 347–357
- Plummer, H. C. 1911, MNRAS, 71, 460
- Prada, F., Klypin, A. A., Simonneau, E., et al. 2006, ApJ, 645, 1001
- Spergel, D. N., Bean, R., Doré, O., et al. 2007, ApJS, 170, 377

- Spitzer, L. 1987, Dynamical evolution of globular clusters (Princeton, NJ, Princeton University Press, 1987, 191 p.)
- Springel, V., Frenk, C. S., & White, S. D. M. 2006, *Nature*, 440, 1137
- Taniguchi, Y., Trentham, N., & Ikeuchi, S. 1999, *ApJ*, 526, L13
- Tout, C. A., Aarseth, S. J., Pols, O. R., & Eggleton, P. P. 1997, *MNRAS*, 291, 732
- von Hoerner, S. 1957, *ApJ*, 125, 451
- White, S. D. M. & Rees, M. J. 1978, *MNRAS*, 183, 341
- Xue, X. ., Rix, H. ., Zhao, G., et al. 2008, *ArXiv e-prints*, 801